

CHAPTER 4

Theoretical Modelling of Multivalent Ions in Inorganic Hosts

GOPALAKRISHNAN SAI GAUTAM^{*a} AND PIEREMANUELE CANEPA^{*b}

^aDepartment of Mechanical and Aerospace Engineering, Princeton University, Princeton, New Jersey 08544, USA; ^bDepartment of Materials Science and Engineering, National University of Singapore, Singapore 117575, Singapore

*E-mail: gautam91@princeton.edu, pcaneпа@nus.edu.sg

4.1 Introduction

The design of multivalent batteries, specifically Mg batteries, has proven to be challenging for a number of reasons: (i) a lack of high voltage cathode materials with good mobility of Mg ions;^{1–5} (ii) a lack of electrolytes that are compatible with the Mg metal anode and high-voltage cathode materials;^{6–8} (iii) poor understanding of metal plating/stripping at the anode;^{6,9,10} and (iv) a lack of standard protocols to perform experiments.⁵

Theoretical calculations, which can be thought of as controlled experiments, are ideal to tackle some of the aforementioned issues, as they limit the number of variables affecting the observables. This chapter will focus on the application of theoretical tools, especially using density functional theory (DFT), to identify Mg cathodes with good intrinsic ionic mobility and

high voltage. We will begin by discussing the thermodynamic and kinetic principles that are used in conjunction with DFT to accurately predict: (i) the intercalation (and conversion) voltages of multivalent electrodes, (ii) the migration barrier of Mg^{2+} ions in host materials, and (iii) the identification of good electrode coatings. We conclude by providing a number of examples of successful applications to topical materials in the Mg chemical space.

4.1.1 Thermodynamics of Multivalent Electrodes

Here, we explore the thermodynamic quantities accessible using DFT in a typical intercalating battery system. We define the Nernst equation for calculating voltages and the subsequent extensions of it to solvent co-intercalating systems, conversion reactions, and electrolyte stabilities.

A reversible reaction of Mg intercalation, where the source of intercalant atoms is from a Mg-metal anode, within a MO_z cathode host (M = redox-active transition metal) is written as:



The intercalation reaction of eqn (4.1) is thermodynamically favoured, if its Gibbs energy, ΔG , is negative (see below).

$$\Delta G \equiv G_{\text{Mg}_x\text{MO}_z} - G_{\text{MO}_z} - xG_{\text{Mg}} \leq 0 \quad (4.2)$$

Subsequently, the Nernst equation of eqn (4.3) can be used to define a change in the electrochemical potential (ΔV) of any reaction, given its Gibbs energy change (ΔG), the number of electrons transferred (n) and the Faraday constant (F).

$$\Delta V = -\frac{\Delta G}{nF}, \quad (4.3)$$

Combining eqn (4.2) and (4.3), we define the average equilibrium voltage for intercalating x moles of Mg into the MO_z host as:

$$\Delta V = -\frac{G_{\text{Mg}_x\text{MO}_z} - G_{\text{MO}_z} - xG_{\text{Mg}}}{2xF} \quad (4.4)$$

Note that each Mg atom corresponds to a transfer of 2 electrons, which explains the factor of 2 in the denominator of eqn (4.4). Additionally, eqn (4.4) is referenced to as the Gibbs energy of Mg metal (G_{Mg}), which sets a natural reference to ΔV as the standard reduction potential (SRP) of Mg metal, which is -2.37 V vs. the standard hydrogen electrode (SHE). Thus, ΔV in eqn (4.4) is always defined with respect to the SRP of Mg^{2+}/Mg . Cathode frameworks that thermodynamically favour Mg intercalation will exhibit a positive ΔV in eqn (4.4). In other words, the anode-(electrolyte) -cathode combination will pump electrical energy into the external circuit, or undergo

“discharge”, during Mg intercalation, if ΔV is positive. Subsequently, the battery will undergo “charge” or will absorb energy from an external power source (equivalent to ΔV), while Mg ions are de-intercalated. In battery literature, Mg_xMO_z and MO_z are often taken as discharged and charged compositions, respectively. Further, the difference between the Gibbs energies of the intercalated and empty cathode in eqn (4.4), *i.e.* $G_{\text{Mg}_x\text{MO}_z} - G_{\text{MO}_z}$, is the change in the chemical potential of Mg (μ^{Mg}) within the cathode host, across the Mg_xMO_z and MO_z concentrations.¹¹ Hence, eqn (4.4) can be generalized to define the equilibrium voltage ($V(x)$ vs. Mg^{2+}/Mg) of a cathode host at a given Mg concentration (x), using eqn (4.5):

$$V(x) = -\frac{\mu_{\text{Mg}_x\text{MO}_z}^{\text{Mg}}(x) - \mu_{\text{Mg}}^{\text{Mg}}}{2F} \quad (4.5)$$

First-principles calculations, such as those based on DFT,^{12,13} are used to calculate the average intercalation voltage (ΔV from eqn (4.4)), for intercalating compositions, x and $x + \Delta x$, while approximating the Gibbs energies of the cathode and the anode to the internal energies at 0 K ($G \approx E$), which are directly obtained from total energy calculations using DFT, resulting in eqn (4.6).

$$\Delta V \approx -\frac{E_{\text{Mg}_{x+\Delta x}\text{MO}_z} - E_{\text{Mg}_x\text{MO}_z} - \Delta x E_{\text{Mg}}}{2\Delta x F} \quad (4.6)$$

Eqn (4.6) includes important approximations, which are often justified, but do play a role while directly comparing DFT calculated with an experimental ΔV , where the experiment is typically done at 298 K and 1 atm. For example, the contributions arising from the volume change as intercalation occurs within the cathode (or an intercalation anode) host, *i.e.* $p\Delta V$, are typically neglected since such contributions are in the order of 10^{-5} eV for most materials, whereas the change in internal energies are in the order of a few (1–10) eV.¹¹ Similarly, the changes in entropy within the cathode host, *i.e.* $T\Delta S \approx 0.01 - 0.1$ eV, are also often neglected. However, entropy changes can influence the phase behaviour of a given cathode host during an intercalation reaction, as discussed in Section 4.1.2. In particular, entropy contributions dominate in determining the ground-state (or equilibrium) crystal structure (or atomic configuration) at higher temperatures. However, the computational cost of calculations required to capture entropy contributions are significant, with most theoretical studies using the calculated ΔV at 0 K to screen for promising cathodes.

4.1.1.1 Ground State Hull, Metastability and Average Voltages

Reversible intercalation reactions are typically “topotactic” processes, where the structural framework at the intercalated and empty compositions remain identical, with the intercalant occupying well-defined vacant sites within the cathode. For example, when Mg reversibly (de-)intercalates into a MO_2 host,

the cathode structure remains identical to that of either the MgMO_2 (fully intercalated) or MO_2 (fully empty) structures, while Mg is removed or added. The framework that the cathode adopts during topotactic intercalation depends on the structure with which the (de-)intercalation process is begun, *i.e.* a fully intercalated (empty) framework is adopted if MgMO_2 (MO_2) is the starting composition. Thus, the calculated intercalation voltage is heavily dependent on the cathode structure (or polymorph) of (de-)intercalation. Given eqn (4.6), the lower (higher) the energy of the intercalated (empty) cathode host, the higher the average voltage.

Since polymorphism plays an important role in determining (de-)intercalation voltages, it is crucial to determine the ground state structures as a function of various intercalant compositions within the cathode framework. Accurate (de-)intercalation voltages (eqn (4.6)) can be estimated from DFT calculations if accurate 0 K phase diagrams, also referred to as “ground state hulls”, can be determined, as schematically illustrated for a hypothetical Mg-intercalation system in Figure 4.1a,b. The term *ground state hull* comes from

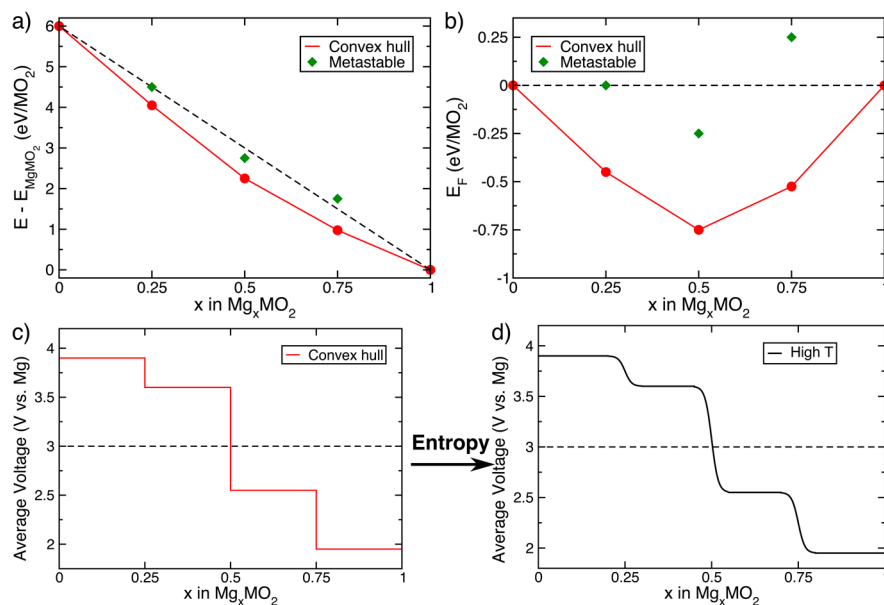


Figure 4.1 (a) The energy landscape in a hypothetical Mg intercalation material, where the energies are referenced to the intercalated composition, MgMO_2 . (b) The ground state hull of the Mg intercalation system, with the energies referenced to both the intercalated and empty (MO_2) compositions. The red lines, red circles, and the green diamonds are the convex (or ground state) hull at 0 K, the ground states and metastable states, respectively. (c) The average voltage curve plotted as a function of Mg concentration (x) for Mg (de-)intercalation in Mg_xMO_2 , obtained from the convex hull of panels (a) and (b), at 0 K. (d) Average voltage curve at a higher temperature including entropic contributions.

the fact that 0 K phase diagrams resemble convex hulls (see Figure 4.1b), since the ground state structure, at a given composition, always minimizes the Gibbs energy at that composition. Thus, given a set of compositions, structures, and Gibbs energies, the equilibrium phase diagram is mathematically obtained through a procedure of convex minimization. Once the ground state hull is obtained, eqn (4.6) is applied to calculate average voltages in a range of compositions, as shown in Figure 4.1c.

In Figure 4.1a, the internal energies are referenced with respect to the fully intercalated composition, *i.e.* E_{MgMO_2} , and the “uphill” nature of the energy landscape indicates the energy required (or the voltage to be applied) to deintercalate Mg^{2+} ions from the MgMO_2 framework. For example, an uphill energy difference of ~ 6 eV between MO_2 and MgMO_2 signifies an average voltage of ~ 3 V *vs.* Mg (see eqn (4.6)) that will be required to charge MgMO_2 completely to MO_2 . Visualizing ground state hulls for intercalating compositions is more intuitive if the energies of intermediate compositions, *i.e.* $0 < x < 1$ for x in Mg_xMO_2 , are referenced to both the discharged (E_{MgMO_2}) and charged (E_{MO_2}) compositions, as shown in Figure 4.1b. Such a representation also allows an intuitive understanding of the metastability of various configurations, shown as the green diamonds in Figure 4.1b, where the metastability of each structure is quantified by the energy above the hull (E^{hull}). Mathematically, the E^{hull} at a given composition is defined as the energy released upon decomposition into the thermodynamic ground state, *i.e.* the distance to the ground state hull. For example, the energy of the metastable configuration at $x = 0.5$ in Figure 4.1b is ~ -0.25 eV/ MO_2 , while the energy of the ground state configuration at the same composition is ~ -0.75 eV/ MO_2 . Hence, the E^{hull} for the aforementioned configuration is ~ 0.5 eV/ MO_2 . Thus, $E^{\text{hull}} \geq 0$, with ground state configurations exhibiting $E^{\text{hull}} = 0$. Although metastable configurations at a given temperature should not exist, entropic or kinetic contributions can stabilize such configurations.

For the Mg_xMO_2 system shown in Figure 4.1, there are three thermodynamically stable configurations at $x_{\text{Mg}} = 0.25, 0.5,$ and 0.75 , as illustrated by the red circles in panels a and b. Since the Mg concentration is the only changing variable in the Mg_xMO_2 system, it can be treated as a (pseudo-)binary system. Note that the Gibbs phase rule in binary systems (at a given T, p) restricts the number of independent variables, which includes μ_{Mg} , to 1 in a single-phase (or ground state) region (red circles in Figure 4.1b), while there are no independent variables in a two-phase region (red lines in Figure 4.1b). Thus, μ_{Mg} , which is related to the average voltages *via* eqn (4.5), either exhibits a continuous range at ground state configurations ($x_{\text{Mg}} = 0.25, 0.5,$ and 0.75) or a single value in two phase regions ($0.75 < x < 1, 0.5 < x < 0.75, 0.25 < x < 0.5,$ and $0 < x < 0.25$). Consequently, the voltage profile in Figure 4.1c exhibits a “jump” across single-phase regions and a “plateau” across two-phase regions. Note that the voltage illustrations in Figure 4.1c are strictly applicable to 0 K, or for single-phases which do not exhibit any composition ranges.

Typically, by including entropy contributions, such as configurational, vibrational, *etc.*, (see Section 4.1.2) in intercalation solids extends the

composition range over which a given phase is stable. For example, the Mg-vacancy configuration that forms the ground state at $x_{\text{Mg}} = 0.5$ in Figure 4.1b is stable only at $x = 0.5$ at 0 K. However, at a higher temperature, the $\text{Mg}_{0.5}\text{MO}_2$ ground state might be stable over a composition range around $x_{\text{Mg}} = 0.5$, say $0.45 \leq x \leq 0.55$. Consequently, the voltage profiles of Mg (de-)intercalation calculated at 0 K (Figure 4.1c) will change at higher temperatures (Figure 4.1d). While the voltage jumps are discrete at 0 K and will happen across distinct ground state compositions, the jumps are continuous and will occur across the range of stable compositions for each stable phase at higher temperatures. Thus, voltage profiles at higher temperatures will appear “smeared” compared to 0 K, with regions of smoothly sloped voltage curves indicating a “solid solution” behaviour.

4.1.1.2 Capturing Entropy Contributions and the Method of Cluster Expansion

Entropy contributions, including vibrational, configurational, magnetic, electronic, *etc.*, which are ignored in eqn (4.6), are important in determining the overall phase behaviour and the resultant voltage profiles. More importantly, entropy differences among solid phases determine which phase is stable at a given temperature. For example, consider a case where two metallic phases A and B in a given system exhibit relatively high but identical amounts of electronic entropy (*i.e.* low G). However, A will be preferentially stabilized at higher temperatures if A exhibits a marginally higher vibrational entropy than B, *i.e.* $S_A > S_B$. Among entropy contributions, vibrational and configurational are important since they can be appreciably different among solid phases, and can selectively stabilize a specific phase at higher temperatures. Capturing either vibrational or configurational entropy requires additional DFT calculations, requiring both significant computational and human time to obtain accurate estimates.

Vibrational entropy in solids can be estimated within the framework of phonons, *i.e.* by combining principles of statistical mechanics with phonon dynamics. In terms of DFT calculations, the phonon density of states (Figure 4.2a displays the density of states for a hypothetical cathode) and the phonon band structure of solids are calculated by obtaining the energies and forces corresponding to different symmetrically-distinct atomic displacements within a supercell of the solid. Subsequently, by calculating the force constants (weighed by the atomic masses) that correspond to various atomic displacements, the phonon properties and the resultant vibrational specific heat (C_v), vibrational entropy (S) and the vibrational Gibbs energies (G , plotted in Figure 4.2b) are estimated.^{14–16} The contribution of phonons is almost insignificant to differences in the vibrational Gibbs energy between most solid phases at low temperatures,¹⁷ *i.e.* $0 < T < 300$ K, justifying why DFT estimates of average voltages do not include phonon contributions. Note that the vibrational thermodynamic properties have to

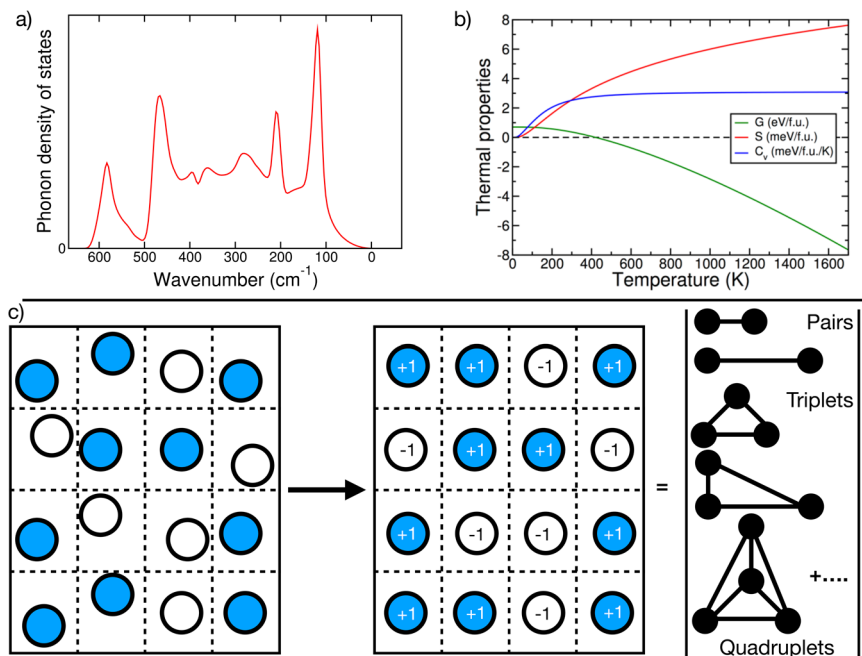


Figure 4.2 (a) Phonon density of states of a cathode material, and (b) computable thermodynamic properties, including the vibrational specific heat (blue curve), vibrational entropy (red), and vibrational Gibbs energy (green). (c) Schematic of the Ising model used to parameterize energies of a given configuration of Mg-ions (blue circles) and vacancies (white circles). Spin values of +1 (−1) are assigned to Mg-ions (vacancies). The energy of each configuration is decomposed to interactions of different clusters, such as pairs, triplets, quadruplets, *etc.*

be added to other entropy contributions to obtain overall thermodynamic quantities. In particular, the vibrational Gibbs energy has to be added to the internal energy (E), pressure–volume contributions ($p\Delta V$), configurational free energy (G_{config}), *etc.* to obtain the overall Gibbs energy of the solid phase.

Configurational entropy is important since the intercalant ions (and corresponding intercalant vacancies) can adopt various configurations within the cathode framework during (de-)intercalation, where several intercalant–vacancy configurations tend to be metastable at 0 K. A pathway to include the configurational entropy in solids is to use a sampling technique over an ensemble of microstates, such as Monte Carlo simulations to evaluate the energies of several possible configurations within the cathode, with the assumption that the cathode system is ergodic. Subsequently, we can use principles of statistical mechanics to obtain ensemble-averaged macroscopic quantities, such as the configurational Gibbs energy. However, performing Monte Carlo simulations on a large set of possible configurations requires

the rapid evaluation of the energies of various configurations to ensure that the process is computationally tractable. Hence, the energy of different configurations within the intercalant systems can be parameterized by a generalized Ising model, often referred to as a “cluster expansion” (CE),^{18,19} which in turn enables computationally feasible Monte Carlo simulations. Apart from energies, CE can be used to parameterize any configuration-dependent properties, such as forces, stresses, *etc.*²⁰

A schematic of the Ising model is provided in Figure 4.2c, where a given configuration (σ) of intercalant atoms (blue circles) and vacancies (white circles) is mapped to an idealized cathode lattice, *i.e.* the energy of the configuration is coarse-grained over any microscopic atomic displacements. Each site is assigned a spin value, namely, +1 and -1 for the intercalant ion and the vacancy (centre panel in Figure 4.2c). Subsequently, the energy (or another property of interest) of the configuration ($E(\sigma)$), as evaluated using DFT, is decomposed into contributions from various clusters, such as pairs, triplets, quadruplets, *etc.* Thus, the CE is written as a summation of the interactions of symmetrically distinct clusters (α), as in eqn (4.7).

$$E(\sigma) = \sum_{\alpha} m_{\alpha} V_{\alpha} \left\langle \prod_{i \in \beta} \sigma_i \right\rangle. \quad (4.7)$$

$E(\sigma)$ in eqn (4.7) can be represented exactly if the summation over α is extended to an infinite number of clusters. In practice, the summation is truncated to a few clusters, with their corresponding effective cluster interactions (ECIs, V_{α} in eqn (4.7)) determined by suitably fitting the energies of multiple configurations ($E(\sigma^1)$, $E(\sigma^2)$, *etc.*). m_{α} is the multiplicity of a given cluster within the structure. σ_i is the occupation variable (± 1) of each site within a cluster, which in turn is averaged over all clusters β that are symmetrically equivalent to α . For example, a pair term (β_1) containing a Mg^{2+} and a vacancy will have a value $\prod_{i \in \beta} \sigma_i = +1 \times -1 = -1$, while another pair (β_2) containing only Mg^{2+} ions will have a value of +1. If β_1 and β_2 are symmetrically equivalent and form a subset of α , then $\left\langle \prod_{i \in \beta} \sigma_i \right\rangle = \frac{-1+1}{2} = 0$, with m_{α} being 2 in this case. Finally, a CE fit to several possible configurations to obtain a reliable set of V_{α} can be used in conjunction with Monte Carlo simulations to obtain the configurational component of the Gibbs energy.

Note that configurational entropy contributions will not affect the overall average voltage normally (*i.e.* between MO_2 and MgMO_2 , dashed black lines in Figure 4.1c,d), since the MO_2 and MgMO_2 ground states will not exhibit multiple Mg-vacancy configurations and will not exhibit a configurational entropy (there are exceptions, where MgMO_2 exhibits multiple possible configurations). However, significant vibrational entropy can change the Gibbs energies of both MO_2 and MgMO_2 and as a result, change the overall average voltage.

4.1.1.3 Conversion vs. Intercalation

When a MO_2 (or equivalently M_2O_4) cathode is reduced by Mg^{2+} , *i.e.* the cathode undergoes discharge, the host can either undergo a reversible intercalation that results in the formation of MgM_2O_4 or an irreversible conversion that results in the formation of decomposition products. In general, conversion reactions are driven by the thermodynamic driving force to form binary compounds, such as MgO and M_2O_3 , MO , *etc.* Conversion reactions are especially exacerbated within Mg-based systems since Mg exhibits a large driving force to form MgO , as quantified by the MgO formation voltage of ~ 3.1 V vs. Mg. Furthermore, MgO formation stops any further electrochemical reactions due to its high stability and poor Mg^{2+} mobility.⁵ Thus, intercalation reactions involving Mg^{2+} always have to compete against conversion reactions during discharge.

To quantify the ability of a cathode host to resist conversion reactions, a thermodynamic framework can be built upon the calculated ground state hull of Figure 4.3 (see Section 4.1.1).²¹ Using DFT, one can calculate the energy ($G \approx E$) of multiple polymorphs of charged (M_2O_4) and discharged (MgM_2O_4) compositions and subsequently identify the lowest energy polymorphs in each scenario. For example, the lowest energy charged (discharged) polymorph in Figure 4.3 is labelled α (λ). The lowest energy polymorphs are the most relevant for calculating intercalation voltages as they exhibit the highest likelihood to be synthesized in experiments. Since intercalation reactions are ideally topotactic, we can define intercalation voltages for both the lowest energy charged and discharged polymorphs, labelled as $V_{\text{int}}^{(\text{charged})}$ and $V_{\text{int}}^{(\text{discharged})}$ (green arrows in Figure 4.3). Given the relationship of voltages to energies *via* eqn (4.6), $V_{\text{int}}^{(\text{discharged})}$ is always higher than (or at least equal to) $V_{\text{int}}^{(\text{charged})}$.

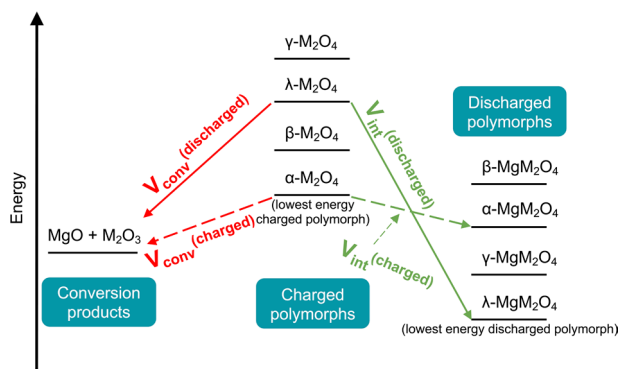


Figure 4.3 Thermodynamic framework to evaluate intercalation and conversion reactions for Mg reduction in typical cathode compositions, M_2O_4 ($\text{M} = 3\text{d}$ transition metal). The lowest energy charged (empty) and discharged (intercalated) polymorphs are the important structures to evaluate topotactic intercalation and possible conversion voltages.

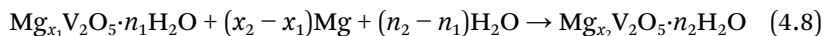
Similar to intercalation reactions starting with α and λ polymorphs, we can calculate the voltages for conversion reactions (red arrows in Figure 4.3) that lead to decomposition products, with different structures and compositions compared to either M_2O_4 or MgM_2O_4 . The precise decomposition products that can form from a potential conversion reaction can be identified based on the ground state hull of the entire Mg–M–O phase space. For example, Mg reduction of M_2O_4 can lead to MgO and M_2O_3 during a conversion reaction, if they are the thermodynamically stable oxides that exist in the $Mg_xM_2O_4$ ($0 \leq x \leq 1$) region of the Mg–M–O ternary phase diagram.

Based on the calculated intercalation and conversion voltages for the lowest energy polymorphs, we can identify which reaction is thermodynamically favoured. Since we are considering scenarios of Mg reduction or discharge into a M_2O_4 cathode host, the reaction exhibiting the higher voltage vs. Mg will be favoured. For example, if $V_{\text{int}}^{(\text{discharged})} > V_{\text{conv}}^{(\text{discharged})}$, then the intercalation process is favoured and will likely occur. Similarly, if $V_{\text{conv}}^{(\text{charged})} > V_{\text{int}}^{(\text{charged})}$, the conversion reaction will likely occur. Notably, a given cathode composition (M_2O_4) can thermodynamically favour the intercalation process with a certain polymorph (say λ), while favouring the conversion reaction with another (α). Nevertheless, the framework displayed in Figure 4.3 is strictly thermodynamic ignoring any kinetic factors that may influence a given intercalation (or conversion) reaction.

4.1.1.4 Solvent Co-intercalation

Since poor Mg^{2+} mobility within bulk oxide frameworks is a major challenge in developing reversible Mg intercalation batteries, intercalated solvent molecules that can electrostatically “shield” the intercalating Mg^{2+} and increase the bulk Mg mobility may improve the performance of a cathode. Several experimental studies have demonstrated superior cycling performance with layered cathodes (e.g. xerogel- V_2O_5) that contain or that co-intercalate solvating water molecules alongside Mg^{2+} -ions. However, changes in the water (or an equivalent solvent) concentration within the cathode structure and the electrolyte can have a significant impact on the voltages measured, phase behaviour of the cathode, and the overall cycling performance. It is important to quantify the impact of solvent co-intercalation on measured voltages in cathode materials that can accommodate solvent molecules, which requires generalizing the voltage expressions of eqn (4.4) and (4.6).

Consider the process of Mg- H_2O co-intercalation within the xerogel- V_2O_5 cathode, which follows eqn (4.8).²²



The voltage for the co-intercalation process can be written, similar to eqn (4.6), as

$$\Delta V = - \frac{\Phi_{Mg_{x_2}V_2O_5 \cdot n_2H_2O} - \Phi_{Mg_{x_1}V_2O_5 \cdot n_1H_2O} - (x_2 - x_1)G_{Mg}}{2(x_2 - x_1)F} \quad (4.9)$$

Φ in eqn (4.9) is the grand-potential of the cathode framework, which accounts for the chemical potential of the solvent molecule that undergoes intercalation. Φ for a given $\text{Mg}_x\text{V}_2\text{O}_5 \cdot n\text{H}_2\text{O}$ composition is defined as,

$$\Phi = G_{\text{Mg}_x\text{V}_2\text{O}_5 \cdot n\text{H}_2\text{O}} - n_{\text{H}_2\text{O}}\mu_{\text{H}_2\text{O}} \quad (4.10)$$

G , $n_{\text{H}_2\text{O}}$, and $\mu_{\text{H}_2\text{O}}$ in eqn (4.10) are the Gibbs energy of the cathode composition, the number of water (or solvent) molecules within the cathode framework, and the chemical potential of water, respectively. Thus, eqn (4.9) is identical to eqn (4.6) when $n_2 = n_1$. While G is obtained from DFT calculations ($G \approx E$), the electrolyte acts as the chemical reservoir for solvent molecules, *i.e.* sets $\mu_{\text{H}_2\text{O}}$, similar to the anode being the reservoir for the intercalating Mg. If the activity of water ($a_{\text{H}_2\text{O}}$) within a given electrolyte is known *a priori*, then $\mu_{\text{H}_2\text{O}}$ can be obtained *via* eqn (4.11). For example, $a_{\text{H}_2\text{O}}$ in a “wet” electrolyte (~ 1) should be several orders of magnitude higher than a “dry” electrolyte ($\sim 10^{-4}$), signifying $a_{\text{H}_2\text{O}}$ as a unique handle that spans various electrolytic conditions.

$$\mu_{\text{H}_2\text{O}} = \mu_{\text{H}_2\text{O}}^0 + RT \ln a_{\text{H}_2\text{O}} \quad (4.11)$$

$\mu_{\text{H}_2\text{O}}^0$ in eqn (4.11) is the chemical potential of water in its standard state, which can be obtained by combining theory calculations and experimental data, as in eqn (4.12) and (4.13). For example, the enthalpy of water vapor (or ice) can be approximated from total energy DFT calculations ($H \approx E$) of an isolated vapor molecule (ice unit cell). Subsequently, the DFT data can be combined with the experimental enthalpy of vaporization (melting) and the entropy of liquid water to obtain an accurate $\mu_{\text{H}_2\text{O}}^0$ at a given temperature (T).

$$\mu_{\text{H}_2\text{O}}^0 = E_{\text{vapor}}^{\text{DFT}} - \Delta H_{\text{H}_2\text{O}}^{\text{vaporization}}(\text{exp.}) - TS_{\text{H}_2\text{O}}^{\text{liquid}}(\text{exp.}) \quad (4.12)$$

$$\mu_{\text{H}_2\text{O}}^0 = E_{\text{ice}}^{\text{DFT}} + \Delta H_{\text{H}_2\text{O}}^{\text{melting}}(\text{exp.}) - TS_{\text{H}_2\text{O}}^{\text{liquid}}(\text{exp.}) \quad (4.13)$$

Combining eqn (4.9)–(4.13), one can estimate the impact of solvent co-intercalation on the average intercalating voltage within a co-intercalating cathode framework, at various Mg compositions and electrolytic conditions.

4.1.1.5 Stability Windows

An ideal electrolyte in a battery system has to remain electrochemically compatible with the anode and the cathode, *i.e.* it should not cause any performance-limiting decomposition products. However, being compatible with the electrodes requires the electrolyte to remain chemically inert, while conducting the redox species through it, over a large range of energies. For example, a Mg battery that exhibits an average voltage of ~ 2.5 V requires an electrolyte that can withstand a change in μ_{Mg} of ~ 5 eV across

the electrodes. As demonstrated for Li-ion systems,²³ solid electrolytes often exhibit a lower range of energies over which they are stable compared to liquids. Thus, it is crucial to quantify (and subsequently predict) the electrochemical stability range of candidate (solid) electrolytes while designing a battery system.

Thermodynamically, a Mg-electrolyte can either be reduced by transfer of Mg atoms from the anode (*i.e.* electrochemical reduction) or to the cathode (electrochemical oxidation). In turn, the reduction and oxidation of the electrolyte will occur at well-defined voltages *vs.* Mg, nominally referred to as the reductive (or cathodic) and oxidative (or anodic) stability limits. Subsequently, the net voltage difference between the cathodic and anodic stability limits defines the electrochemical stability window (ESW) of an electrolyte. To a first order of approximation in liquid electrolytes, the stability window is given by the position of the lowest unoccupied molecular orbital (LUMO, relevant for reduction) and the highest occupied molecular orbital (HOMO, oxidation) levels, with respect to a Mg metal reference. More generally, the stability window depends on the range of Mg chemical potentials that the electrolyte is stable across.

To estimate the ESW of an electrolyte, we use eqn (4.14), where Φ , G , n , and μ are the grand-canonical potential, the Gibbs energy ($G \approx E$), number of Mg atoms within the electrolyte phase (c), and the Mg chemical potential, respectively.²³

$$\Phi[c, \mu_{\text{Mg}}] = G[c] - n_{\text{Mg}}[c] \mu_{\text{Mg}} \quad (4.14)$$

We can estimate the range of μ_{Mg} that the electrolyte is stable across, given the relevant 0 K phase diagram is calculated. For example, we can use eqn (4.14) to estimate the ESW of a solid Mg-ionic conductor, MgSc_2Se_4 ,²⁴ once we calculate the ternary Mg–Sc–Se phase diagram at 0 K. In case a specific electrode–electrolyte combination gives rise to complex interfacial reactions that may alter the stability limit of the electrolyte//electrode interface, eqn (4.14) has to be extended to include the entire electrode (e) and electrolyte (c) chemical space, as in eqn (4.15), where x is the degree of mixing between the electrode and electrolyte ($0 \leq x \leq 1$).

$$\Phi[c, e, \mu_{\text{Mg}}] = \min(xG[c] + (1-x)G[e]) - n_{\text{Mg}}[xc + (1-x)e] \mu_{\text{Mg}} \quad (4.15)$$

where $\min(xG[c] + (1-x)G[e])$ and $n_{\text{Mg}}[xc + (1-x)e]$ in eqn (4.15) refer to the lowest Gibbs energy within the electrode–electrolyte phase space, and the number of Mg atoms, respectively, at the mixing fraction, x . Thus, to estimate the oxidative stability of MgSc_2Se_4 conductor in contact with a MgTi_2S_4 cathode, we need to (i) calculate the entire Mg–Sc–Se–Ti–S phase-diagram with DFT at 0 K, (ii) consider possible interfacial products for different degrees of MgSc_2Se_4 – MgTi_2S_4 mixing, and (iii) compute the oxidative stability for the resultant interfacial products, which will in turn determine the overall oxidative stability of the MgSc_2Se_4 electrolyte against MgTi_2S_4 . Nevertheless,

kinetic barriers involved in the oxidation or reduction processes can cause significant deviations from the thermodynamic estimates made using eqn (4.14) or (4.15).

4.1.2 Kinetics of Ionic Diffusion in Materials

In this section, we discuss the foundations of ion transport in solids and the derivation of the principal quantities that can be calculated from first-principles. We start by assuming that ionic motion in battery materials follows Fick's first law (Section 4.2.1) and arrive at the definition of the diffusion coefficient through the Green–Kubo relationship. We conclude by connecting the diffusion coefficient with the activation barrier for ionic migration, which is used in screening host materials for adequate ion transport.

4.1.2.1 Fick's First Law and the Green–Kubo Model for Diffusion

Under the assumption of steady state, Fick's first law of eqn (4.16) can be used to describe the flux (\mathbf{J}) of ionic species in solids across a concentration gradient ($\vec{\nabla}C$).²⁵

$$\mathbf{J} = -D_c \vec{\nabla}C \quad (4.16)$$

where D_c is the tensorial diffusion coefficient measuring the mobility of ions in the host structure, including any anisotropy in ionic motion. At thermodynamic equilibrium, D_c is defined by eqn (4.17).

$$D_c = \Theta D_J \quad (4.17)$$

Θ is the so-called thermodynamic factor, as in eqn (4.18).

$$\Theta = \left(\frac{\langle (\delta N)^2 \rangle}{\langle N \rangle} \right)^{-1} = \left(\frac{\partial \left(\frac{\mu}{kT} \right)}{\partial \ln x} \right) \quad (4.18)$$

where N is the number of diffusing species (e.g. Mg^{2+}), and μ is the chemical potential of the diffusing species at concentration x . Thus, eqn (4.18) indicates that the underlying driving force for ionic diffusion is not the concentration gradient as in eqn (4.16), but the gradient of μ . Under ideal conditions, μ is proportional to $\ln x$, and diffusion is across a $\vec{\nabla}C$ (eqn (4.16)). Notably, $\langle (\delta N)^2 \rangle$ of eqn (4.18) is the fluctuation of the number of mobile species in an open system. For simplicity, we can assume that the system is closed to the exchange of species, and thus $\langle (\delta N)^2 \rangle$ is simply the fluctuation in a region of $\langle N \rangle$ species. Therefore, Θ becomes a function of the spatial configuration of the mobile ions at a specific concentration.

D_J of eqn (4.17) is the jump diffusion coefficient, which is,

$$D_J = \lim_{t \rightarrow \infty} \left[\frac{1}{2dt} \frac{1}{N} \left(\sum_{i=1}^N \bar{r}_i(t) \right)^2 \right], \quad (4.19)$$

where d is the dimensionality of the host where ion i diffuses, while $\bar{r}_i(t)$ is its displacement after a period of time t . Therefore, as species i diffuses in the host material over time t , D_J measures the displacement of the centre of mass of the diffusing species. Altogether, eqn (4.17)–(4.19) form the Green–Kubo model of ionic diffusion. Theoretically, $\bar{r}_i(t)$ is estimated using either molecular dynamics (MD)²⁴ or kinetic Monte Carlo simulations.

Often ionic motion in solids is measured by a tracer species with a diffusion coefficient D^* (eqn (4.20)), which is different from D_J (eqn (4.19)).

$$D^* = \lim_{t \rightarrow \infty} \left[\frac{1}{2dt} \left(\frac{1}{N} \sum_{i=1}^N [\bar{r}_i(t)]^2 \right) \right]. \quad (4.20)$$

D^* tracks the displacement of the individual tracer, as opposed to the centre of mass of the diffusing species in D_J . Importantly, D_J reduces to D^* if the displacements of the species are not correlated over time, *i.e.* diffusing atoms/ions move randomly.

4.1.2.2 Diffusion Coefficients and Activation Barriers

Eqn (4.21) defines the Arrhenius-type relationship between the diffusion coefficient (D_J or simply D , eqn (4.19)) and the activation or migration barrier, ΔE_a , in a crystalline material.

$$D = a^2 g f x_D \nu^* \exp\left(\frac{-\Delta E_a}{kT}\right). \quad (4.21)$$

where a is the hop distance of the migrating ion between two identical crystallographic sites, g is the geometric factor, f is a correlation factor and x_D is the concentration of diffusion carriers (*i.e.* vacancies or interstitials). The hopping frequency of eqn (4.21), ν^* , can be written in terms of the attempt frequency ν that is related to bond vibrations (or phonons) and the activation entropy (ΔS_a), which is the entropy difference between the stable and activated states. For simplicity, ν^* is often assumed to range between 10^{12} and 10^{13} Hz, while vibrational contributions dominate ΔS_a .

$$\nu^* = \nu \exp\left(\frac{\Delta S_a}{k}\right) \quad (4.22)$$

ΔE_a is defined as the energy difference between the initial stable state (E_i in Figure 4.4) and the activated state (E^*), as in eqn (4.23).

$$\Delta E_a = E^* - E_i \quad (4.23)$$

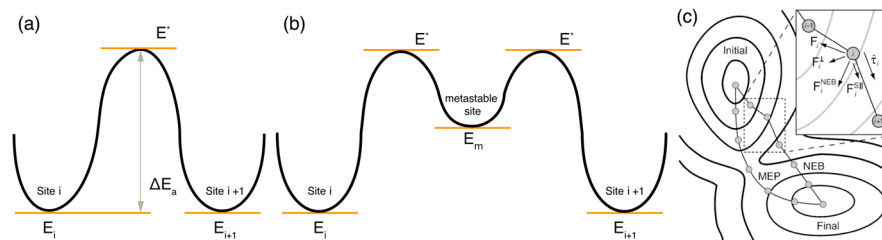


Figure 4.4 Minimum energy path (MEP) experienced by ions moving in a host material in two idealised scenarios (a) plateau-type and (b) valley-type. The initial site is identified by E_i and is separated by a ΔE_a barrier to its equivalent site E_{i+1} or to a metastable site with energy E_m . (c) The starting elastic band of images (grey circles), highlighted by the dashed black square, that converges to the MEP connecting two ground state geometries, *i.e.* initial and final, within the nudged elastic band (NEB) method. The inset indicates the forces that are relevant in NEB, namely, (i) the spring force $F^{\text{S||}}$ acting parallel to the NEB, and (ii) the force perpendicular to the NEB $F^{\text{S}\perp}$ set by the potential energy surface. F^{NEB} is the total force acting along the band. Reproduced from ref. 26 with permission from AIP Publishing, Copyright 2008.

Physically, ΔE_a represents a saddle-point in the energy landscape, *i.e.* it is the *lowest highest* energy state that migrating ions have to cross. The path connecting the stable sites *via* the saddle point is called the minimum energy path (MEP). Figure 4.4 illustrates two ideal scenarios of MEP (black lines) for ionic migration in solids, namely (a) plateau-like, whereby the diffusing ion crosses one activated state while migrating between two stable sites; (b) valley-type, where the ion traverses a metastable site as it migrates between stable sites. For example, a valley-type MEP is found for Li or Mg migration in a spinel- Mn_2O_4 structure,¹ while Li-MEP in a layered- NiO_2 structure is plateau-like.

4.1.2.3 Estimating Migration Barriers

ΔE_a in solids can be (directly or indirectly) measured from a number of experimental techniques, such as impedance spectroscopy, nuclear magnetic resonance (NMR), *etc.* Theoretically, ΔE_a can be estimated from utilizing saddle-point finding algorithms, such as the nudged elastic band (NEB) method,¹ or extrapolated from MD simulations over a range of temperatures.²⁴

The NEB method^{26–28} computes MEPs using an elastic band of geometric configurations, referred to as images (grey circles in Figure 4.4c), that approximate the MEP, *i.e.* each image represents a distinct configuration along the ionic migration. The starting band (dashed black square in Figure 4.4c) is eventually relaxed to the MEP through a force projection scheme, where the force due to the potential energy acts perpendicular (F^{\perp}) to the band, and the spring force ($F^{\text{S||}}$) acts parallel to the band. $F^{\text{S||}}$ ensures (roughly) equal

spacing among images, giving rise to the elastic nature of the band, and aids in obtaining a reliable MEP profile. Thus, the convergence of the starting band to the MEP is done by minimizing the net force, F^{NEB} . Since forces are straightforward to compute in DFT,^{29–31} the NEB method has been extensively used in conjunction with DFT to compute the ΔE_a of ions in solids (see Section 4.4.6).^{1,2,4,32,33}

Nevertheless, reliably predicting MEP is time consuming as each image in the band represents a distinct DFT calculation. Furthermore, a linear interpolation of images between initial and final states may not represent an ideal starting band which can decelerate NEB convergence. Rong *et al.*³⁴ have proposed two strategies to accelerate NEB calculations: (i) The *PathFinder* algorithm, based on the fact that ions in host structures migrate avoiding other atoms or bonds, *i.e.* avoiding regions with dramatic changes of electronic charge densities, and (ii) The *ApproxNEB*, which evaluates the energy of each image within the band using an inexpensive single-point DFT calculation. Thus, *PathFinder* (obtains approximate paths) and *ApproxNEB* (calculates approximate energies) can be used together to approximately predict ΔE_a . An alternative methodology to find approximate MEPs^{35–37} is the bond valence site energy (BVSE) method, which can be thought of as an empirical force field that calculates the energies around various ionic sites. Nishitani *et al.*³⁷ applied the BVSE to Mg^{2+} migration in several hosts reproducing the barriers obtained using costly DFT-NEB calculations. To identify good Mg conductors from large datasets one can employ these inexpensive methods.³⁸

4.1.2.4 Percolation Theory

The migration barriers extracted from structural models, as discussed in Sections 4.2.1 and 4.2.2, provide an atomic picture of ion dynamics. However, macroscopic diffusion of ions in materials relies on the existence of percolating networks of active migration channels, as displayed in Figure 4.5. Hence, in addition to recognizing facile microscopic hops from theory (*e.g.* DFT-NEB), it is important to identify whether a contiguous percolating network of low-barrier migration channels exist, which can be mathematically modelled and predicted by percolation theory. Understanding the existence of percolation networks is paramount to be able to quantify and engineer the extent of usable capacity in electrodes.

Theoretically, the solution to the site percolation problem^{39–41} estimates the critical concentration $x = x_{\text{crit}}$ (also referred to as “percolation threshold”) at which an infinite network of contiguous connected sites exists in a randomly occupied infinite lattice. For example, in Figure 4.5 a minimum of 5 yellow circles is required to form a percolating network (green line) that can span the 2D lattice of 45 blue circles, resulting in an $x_{\text{crit}} = 5/45 = 1/9$. The blue and yellow circles in Figure 4.5 can be considered to be the cathode framework and Mg atoms. Thus, two Mg atoms (yellow circles) are considered to be connected if there is an active Mg migration channel connecting the two sites. x_{crit} defines the critical concentration of Mg atoms

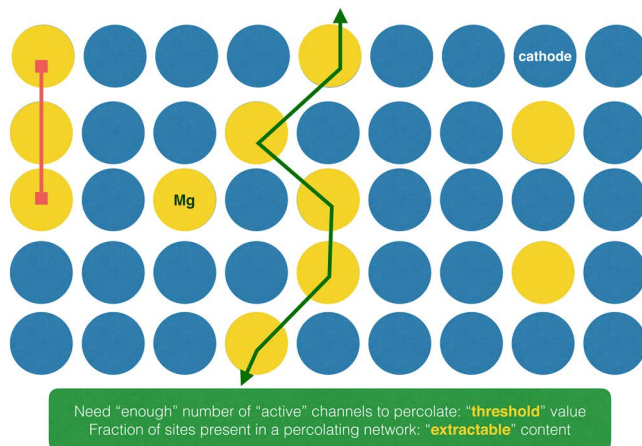


Figure 4.5 Schematic of a 2D lattice of blue circles with a percolating (green line) and a non-percolating (red line) network of contiguous connected yellow circles. The blue (yellow) circles can be considered to be cathode (Mg) atoms of an intercalation framework. The important quantities from percolation theory are listed in the green box at the bottom.

at which enough Mg sites are connected by active migration channels and macroscopic Mg transport is feasible. Thus, the probability that a percolating network exists within a lattice, $p(x)$, exhibits a step-function at x_{crit} , as in eqn (4.24).

$$p(x) = \begin{cases} 0 & \forall x < x_{\text{crit}} \\ 1 & \forall x \geq x_{\text{crit}} \end{cases} \quad (4.24)$$

Percolation thresholds can be analytically derived for 2D lattices.³⁹ However, in 3D lattices, numerical Monte Carlo simulations are used to assess x_{crit} .^{4,41–43} Due to the use of finite supercells with periodic boundary conditions in Monte Carlo simulations (that result in “wrapping effects”), $p(x)$ becomes a sigmoidal functional form. However, Urban *et al.*⁴¹ demonstrated that the inflection point of $p(x)$, defining x_{crit} , does not change significantly due to a change of functional form, and a well-converged x_{crit} can be obtained with computationally tractable 3D supercells. Thus, Monte Carlo simulations can accurately capture the percolation dynamics yielding reliable estimates of x_{crit} for practical cathodes.

Another important quantity accessible from Monte Carlo simulations is the fraction of sites, $F(x)$, participating in the percolating network. For example, although the concentration of yellow circles (x) in Figure 4.5 exceeds x_{crit} , not all yellow circles are connected to the percolating network (green line), with several isolated “clusters” that are connected (red line). Similarly, for $x > x_{\text{crit}}$ in a 3D cathode, each occupied Mg site is either part of a percolating network (and participates in macroscopic diffusion) or is only a part of a finite cluster in isolation. Subsequently, $F(x)$ can be defined as the fraction of the

number of sites in the percolating cluster ($n_{\text{percolating}}(x)$) over the total number of sites in the 3D lattice ($n_{\text{sites}}(x)$), as in eqn (4.25).

$$F(x) = \frac{n_{\text{percolating}}(x)}{n_{\text{sites}}} \approx \frac{1}{n_{\text{sites}} N_{\text{MC}}} \sum_i^{N_{\text{MC}}} n_{\text{percolating}}^i(x) \quad (4.25)$$

In practice, $F(x)$ is averaged over a large number of Monte Carlo sweeps (N_{MC}), where each sweep covers a range of concentrations (x). Importantly, $F(x)$ maps directly to the capacity of a cathode and can be compared immediately to electrochemical measurements.

4.1.3 Density Functional Theory as a Tool to Assess Thermodynamic and Kinetic Properties

While we introduced the thermodynamic and kinetic properties that govern battery materials in Sections 4.1 and 4.2, here we discuss the first-principles methodologies that provide reliable prediction of such properties. Our focus is limited to DFT,^{12,13} which gives an accurate assessment of internal energies (total energies) that are used in the theoretical models presented in Sections 4.1 and 4.2.

In DFT, as in other quantum-mechanical methods, such as Hartree–Fock (HF), Møller–Plesset, coupled cluster, *etc.*,⁴⁴ the total energies are computed by numerically solving the time-independent Schrödinger equation ($H|\psi\rangle = E|\psi\rangle$), which only requires the atomic positions in space as input. The foundation of DFT relies firmly on the Hohenberg and Kohn theorem,¹² which proves that “the full many-particle ground state is a unique functional of $\rho(r)$ ” and that the only the true ground state $\rho(r)$ yields the lowest total energy, where $\rho(r)$ is the electronic charge density. Hence, the Schrödinger wavefunction ($|\psi\rangle$), which depends on the $3(N + M)$ spatial coordinates (N , M = number of electrons, nuclei), is recast in terms of $\rho(r)$ in DFT, which depends only on 3 spatial coordinates (x, y, z) and significantly reduces the computational cost.^{31,44} To simplify the complex description of the charge density of materials with multiple correlated electrons, Kohn and Sham¹³ introduced the concept of a non-interacting electron-gas, *i.e.* electrons do not interact with each other and instead individually interact with a mean-field $\rho(r)$. Thus, the many-electron wavefunction is mapped as a collection of Kohn–Sham (KS) one-electron orbitals. Within this approximation, the charge density of the non-interacting electron-gas is mapped to the ground state density ($\rho(r)$) of the actual interacting electron system, with the ground state energy (E) written as a functional of $\rho(r)$.

$$E[\rho(\vec{r})] = T_s[\rho] + J[\rho] + E_{\text{xc}}[\rho] + \int V_{\text{Ne}} \rho(\vec{r}) d\vec{r}. \quad (4.26)$$

where $T_s[\rho]$ is the kinetic energy of the non-interacting electron gas, $J[\rho]$ is the classical Coulomb repulsion between electrons, and V_{Ne} is the electrostatic potential from the atomic nucleus. The exchange and correlation

(XC) functional, $E_{\text{XC}}[\rho]$, contains non-classical interactions, such as electronic exchange (which follows the Pauli exclusion principle), the difference in kinetic energy between an interacting and a non-interacting electron gas, and static and dynamic interactions of individual electrons that result in correlation effects. Thus, by approximating a many-body wavefunction as a linear combination of KS orbitals, and by solving eqn (4.26) self-consistently, one can obtain a good approximation for the ground state energy of most practical multi-electron systems.

The grand-challenge in DFT, as categorized by Jacobs' ladder,⁴⁵ is to accurately describe the electronic XC whose functional form is unknown. A number of XC functionals have been developed, including the linear density approximation (LDA), where E_{XC} depends on the local $\rho(r)$,⁴⁶ the generalized gradient approximation (GGA)⁴⁷ accounting for local $\rho(r)$ and $\vec{\nabla}\rho(r)$, and meta-GGA functionals that include higher-order gradients of ρ and/or kinetic energy densities. An example of recent meta-GGA functionals is the strongly constrained and appropriately normed (SCAN) functional,⁴⁸ satisfying the 17 known constraints for XC functionals.

4.1.3.1 GGA+U and Hybrid Functionals

The mean-field formulation of DFT does not penalize electrons enough from fictitiously interacting with themselves,⁴⁶ that results in the so-called self-interaction error (SIE), which affects total energy estimates. Particularly in oxides with open-shell 3d or 4f orbitals, which are relevant as intercalating cathodes (*e.g.* LiCoO₂ and LiFePO₄)⁴⁹ the SIE arising from insufficient localization of electrons in the 3d/4f orbitals can be sizable. A number of correction schemes have been proposed to reduce the SIE:

- **DFT+U**– The formalism by Anisimov *et al.*⁵⁰ lowers the SIE in 3d and 4f orbitals by adding an orbital-dependent on-site energy-penalty (U) for fractional occupation of electrons. DFT+U has been successfully applied to describe the thermodynamics of intercalation in several cathodes.^{4,33,49,51–53} Recently, it was reported that the SCAN XC functional also requires a U correction to accurately reproduce the ground state polymorph, electronic structure, and redox energetics of 3d and 4f oxides.⁵⁴
- **Hybrid functionals**– SIE is reduced by adding a finite amount of the exact HF exchange in the XC functional. Two distinct classes of hybrid functionals exist:^{55,56} (i) linear global hybrids, where a portion of the DFT exchange term is replaced by the HF exchange throughout the system, *e.g.* B3LYP^{57–59} and PBE0,⁶⁰ and (ii) range-separated hybrids, where HF exchange is added within selective space domains, *e.g.* HSE06.^{61,62}

The literature presents several examples where using the GGA+U^{63,64} or HSE06⁶⁵ functional significantly improves the prediction of thermodynamic properties (*e.g.* formation energies and intercalation voltages) of oxides

containing open-shell 3d and 4f transition metals compared to semi-local LDA and GGA XC functionals. In general, hybrid functionals are computationally more expensive than GGA+ U calculations, especially when the KS orbitals are written in a plane-wave basis, since the HF exchange-integrals have to be explicitly computed. Therefore, GGA+ U remains the strategy of choice for high-throughput DFT studies.^{2,4,49,51,63,64}

Typically, GGA-based NEB (or molecular dynamics) calculations are used to estimate migration barriers (see Section 4.2.3),^{1,2,4,66} which have been shown to agree satisfactorily with experimental measurements in Li-ion, and Na-ion solid electrolytes.³⁸ However, GGA may not accurately localize electrons within the 3d/4f orbitals within oxide cathodes. For example, Barnes *et al.*⁶⁷ recently reported that Mg²⁺ migration barriers in MnO₃ is significantly underestimated with GGA (~0.92 eV) compared to HSE06 (~1.53 eV). Although GGA+ U can correct the SIE of GGA, the degree of electron localization is expected to vary between the images (or as the ion migrates) within a NEB calculation, which in turn will require different U values for different images. Hence DFT+ U is clearly not suitable for NEB calculations. A plausible alternative is performing NEB calculations using expensive hybrid functionals, where more validation is required with experiments.

4.1.4 Application of First-principles Methods to Multivalent Ion Intercalation Hosts

Our attention turns to the application of the methodologies introduced in Sections 4.1–4.3 to the study of materials relevant for Mg batteries.

4.1.4.1 High-throughput Screening to Identify a Promising Intercalation Motif

The accuracy of DFT together with the availability of high-performance supercomputers, and materials informatics has fuelled a paradigm shift in materials design, thus allowing researchers to screen across material classes by systematic evaluation of properties. The combination of DFT, with pre/post-processing algorithms and databases is referred to as high-throughput screening (HTS), which has been applied² to identify candidate cathodes in a number of multivalent applications, including Al³⁺, Ca²⁺, Mg²⁺, Y³⁺ and Zn²⁺, as demonstrated in Figure 4.6.

Each point in Figure 4.6 represents the computed open circuit voltage of the intercalation MV ions using eqn (4.6), within M₂O₄ (M = 3d transition metal) cathodes that have the spinel structure (see Section 4.4.6). The voltages in Figure 4.6 were computed at the GGA+ U level of theory (see Section 4.3.1). Expectedly, the computed voltages follow the electrochemical series across intercalant species (*i.e.* Li⁺/Li ~ -3.04 V vs. SHE > Ca²⁺/Ca -2.87 V > Mg²⁺/Mg ~ -2.37 V > Y³⁺/Y ~ -2.37 V > Al³⁺/Al ~ -1.67 V > Zn²⁺/Zn ~ -0.76 V), which provides further validation for calculating voltages using GGA+ U . Notably, the multivalent intercalation voltages reported in Figure 4.6 are

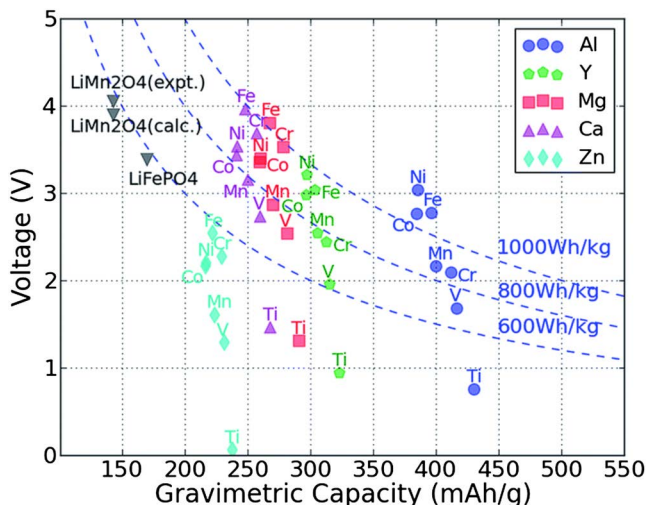


Figure 4.6 Predicted open circuit voltages vs. gravimetric capacities of multivalent ions Al, Ca, Mg, Y and Zn in M_2O_4 spinels (with $M = \text{Mn, Fe, Co, Ni, and Cr}$). Transition metals M are displayed next to each compound. Dashed blue lines are target energy densities, *i.e.* 600, 800, and 1000 Wh kg^{-1} . Reproduced from ref. 2 with permission from the Royal Society of Chemistry.

always lower than 4 V (vs. the corresponding metal), with most Mg and Ca intercalation compounds providing voltages of between 2 and 4 V, which is lower than Li-intercalation within the same hosts. However, considering the additional charge carried by multivalent cations, a multivalent spinel cathode could exhibit a significantly higher energy density than the corresponding Li version.

Apart from computing intercalation voltages, it is important to verify the relative thermodynamic stability of the discharged and charged compositions, by calculating their E^{hull} (see Section 4.1.1), which is readily available on the “Battery Explorer” app^{35,49} in the Materials Project website.⁶⁸ Also included in the app are theoretical (gravimetric and volumetric) capacities and energy densities. It has been estimated by Sun *et al.*⁶⁹ that structures with values of energy above the hull below ~ 70 meV/atom may be accessible *via* specific synthesis procedures even though they are metastable at 0 K.

4.1.4.2 Voltage Curves as a Function of Temperature, the Case of TiS_2 , CrO_2 and V_2O_5

This section emphasizes the predictive power of DFT calculations when coupled with cluster expansion models and statistical thermodynamics. We present the simulated Mg intercalation voltage curves as a function of temperature for three prototypical cathode materials, including, TiS_2 , CrO_2 , and V_2O_5 , which have been the subject of several experimental investigations.^{70–74}

To date, Mg intercalation in spinel-TiS₂, against a Mg metal anode and an aluminium–chloride-based electrolyte, has provided the highest energy density reversible Mg battery.⁷² Figure 4.7 shows the computed phase diagram of Mg intercalation into various polymorphs of TiS₂ for Mg concentrations in the range of $0 < x < 0.5$,⁶⁶ where each point at a Mg composition represents a specific arrangement of Mg and vacancies, or Mg orderings, in TiS₂.

Experimentally, Mg_xTiS₂ exists in two phases, the layered-O1 (blue circles in Figure 4.7), and the spinel (orange). Other layered phases where Mg is coordinated by regular sulphur octahedra (O3) but following a different stacking sequence or prismatic structures (P3/P2) were also investigated in ref. 66. Figure 4.7 shows that Mg favourably intercalates in the TiS₂ framework up to a composition of $x_{\text{Mg}} = 1/2$. The layered-phase (blue), hitting the lowest formation energies, defines the ground state at Mg compositions

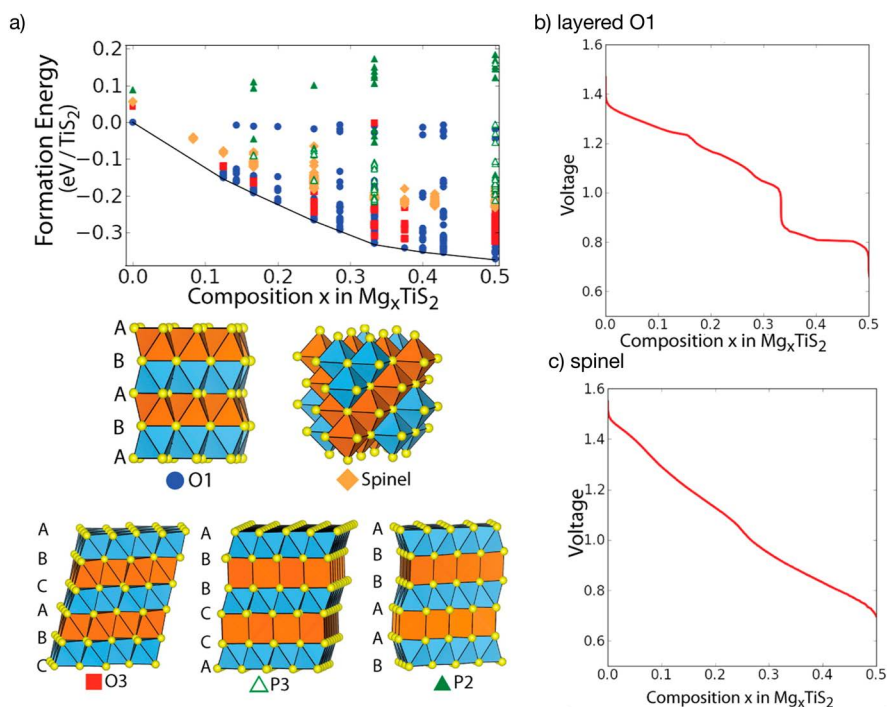


Figure 4.7 (a) Compositional phase diagram computed with DFT at 0 K of Mg intercalation in various phases of TiS₂.⁶⁶ The x -axis shows the Mg composition and y -axis the formation energy vs. empty TiS₂. The orange diamonds indicate the spinel-TiS₂. The red squares and blue circles represent the layered-TiS₂ with octahedrally coordinated Mg and two distinct Ti–S layer stacking. Similarly, empty and filled green triangles indicate layered-TiS₂ as well, where Mg is in a prismatic coordination. Computed voltage curves at 300 K for Mg intercalation in two TiS₂ phases, (b) layered O1 and (c) spinel. Reproduced from ref. 66 with permission from the American Chemical Society, Copyright 2015.

of $0 < x < 0.5$, and is followed in stability by the O3 phases. Experimental observations^{70,72,73} verified that the spinel structure O3 is not ground-state at all. A certain range of Mg compositions and special care is required to intercalate Mg in this polymorph.^{70,72,73} From a visual inspection of the O1 structures, several stable ordered phases can be identified, at $x_{\text{Mg}} = 1/6$, $1/3$ and $1/2$. The ordering at $x_{\text{Mg}} = 1/6$ displays every other Mg layer being completely empty while the remaining alternating layers are $1/3$ occupied. In the case of $\text{Mg}_{1/3}\text{TiS}_2$, every Mg layer is $1/3$ Mg occupied. At $x_{\text{Mg}} = 1/2$, Mg ions order into staggered arrangements of Mg rows (extending in each 2D plane) across different layers of TiS_2 .

Using the energetics of the Mg orderings in TiS_2 (Figure 4.7a) the authors fitted a cluster expansion (see Section 4.1.2), which includes configurational contributions to the Gibbs energy of the Mg_xTiS_2 chemical space. Figure 4.7 shows the voltage profile at 300 K of the Mg_xTiS_2 system, calculated using Monte Carlo simulations based on the cluster expansion, in (b) the layered phase and (c) the spinel phase. The sloping nature of both voltage curves ($0 < x < 0.3$ in layered, and up to $x \sim 0.5$ in spinel) reflects the solid–solution character for Mg intercalation in the TiS_2 phases. In Figure 4.7b, three steps can be identified, corresponding to minima in panel a, which match the Mg orderings at $x_{\text{Mg}} = 1/6$, $1/3$ and $1/2$. In contrast, regions where the voltage curve is smooth reflect the solid–solution behaviour and correspond to regimes of disorder between Mg and vacancies. The spinel phase of Figure 4.7c shows a continuous solid–solution behaviour across Mg compositions, which the authors⁶⁶ attributed to a larger degree of electrostatic screening in the spinel compared to the O1 phase.

$\text{Mg}_x\text{Cr}_2\text{O}_4$ is one of the highest voltage Mg intercalation cathodes as identified from the high-throughput computational screening of Liu *et al.* (Figure 4.6).² To understand the phase behaviour of Cr_2O_4 during Mg intercalation, Chen *et al.*⁵² fitted a cluster expansion (see Section 4.1.2) of the Mg vacancy configurational space within $\text{Mg}_x\text{Cr}_2\text{O}_4$. Subsequently, the authors performed Monte Carlo simulations to quantify changes in the voltage profile during Mg (de-)intercalation, as a function of temperature (Figure 4.8a). A fair agreement between the voltage profile computed by the cluster expansion at 0 K (yellow line of Figure 4.8a) to the DFT version (green line) was found. At room temperature (black line in Figure 4.8a) a fairly smeared voltage profile is obtained with distinct voltage jumps at $x_{\text{Mg}} = 0.5$ and 0.33 . Thus, the Mg vacancy ground states forming at $x_{\text{Mg}} = 0.5$ and 0.33 are energetically stable compared to configurations at other Mg compositions and will exist during (de-)intercalation even under room temperature conditions. The authors demonstrated that ground states at $x_{\text{Mg}} = 0.5$ and 0.33 will curb Mg mobility during Mg (de-)intercalation, attributed to their corresponding stability. At $x_{\text{Mg}} < 0.25$ the steep voltage increase is due to the high instability of the empty spinel- Cr_2O_4 structure, which may potentially lead to decomposition of the spinel structure to a stable Cr_2O_4 polymorph.

In the case of V_2O_5 , Sai Gautam *et al.*⁵³ identified $\delta\text{-V}_2\text{O}_5$ as a promising Mg cathode owing to a combination of a reasonable average voltage (~ 2.5 V) and

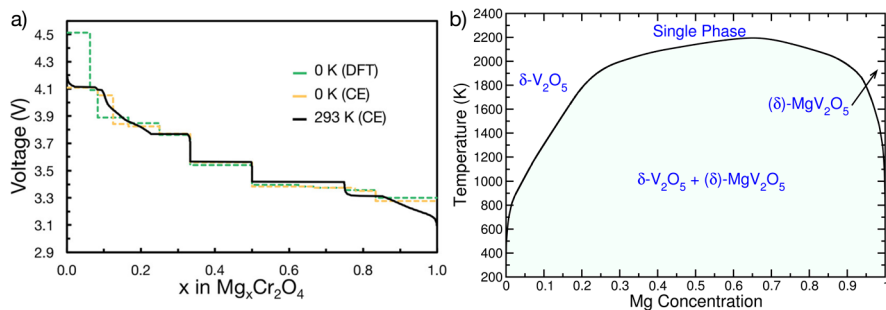


Figure 4.8 (a) 0 and 298 K voltage curves for Mg intercalation in spinel- Cr_2O_4 . Reproduced from ref. 52 with permission from the American Chemical Society, Copyright 2018. (b) Temperature-composition phase diagram for Mg intercalation in $\delta\text{-V}_2\text{O}_5$. Reproduced from ref. 53 with permission from the American Chemical Society, Copyright 2015.

migration barrier (~600–760 meV). Cluster expansion-based Monte Carlo simulations were performed to derive the temperature-composition phase diagram (Figure 4.8b) of Mg intercalation, which indicated that $\delta\text{-Mg}_x\text{V}_2\text{O}_5$ was a phase separating system, with the concomitant formation of Mg-rich and Mg-poor domains. The two-phase behaviour at intermediate Mg compositions ($0 < x < 1$) should exist up to high temperatures (melting point of V_2O_5 ~954 K). Given that the ground state of V_2O_5 is the α polymorph (α is more stable than δ by ~100 meV/f.u.) and the α and δ polymorphs are only separated by a shear transition of alternate V_2O_5 layers, it is crucial for the de-intercalated $\delta\text{-V}_2\text{O}_5$ to remain metastable with Mg (de-)intercalation if $\delta\text{-V}_2\text{O}_5$ is to be successfully used as a practical Mg cathode.

4.1.4.3 Conversion vs. Intercalation During Mg Reduction

Figure 4.9 plots the intercalation vs. conversion reaction voltages for a one electron reduction that involves the reaction of one mole of Mg per mole of M_2X_4 , where M and X are a 3d transition metal and a chalcogen (*i.e.* O, S, Se), respectively.²¹ The polymorph under consideration can exhibit the lowest energy at the intercalated/discharged (left panel in Figure 4.9) or empty/charged (right panel) state (see Section 4.1.3). Blue squares in Figure 4.9 indicate that intercalation is preferred, whereas red squares indicate a conversion preference. From Figure 4.9, it is clear that most 3d sulphides and selenides favour conversion reactions upon Mg reduction. For 3d oxides, when considering the lowest energy discharged polymorph, there are a few compounds that resist conversion reactions, such as oxides of V, Cr, Mn, Fe and Co that favour intercalation over conversion upon Mg reduction. Interestingly, Cr_2O_4 displays the highest level of intercalation preference (or resistance to conversion) among the 3d oxides. However, even among oxides, conversion reactions are favoured during Mg reduction if the lowest energy

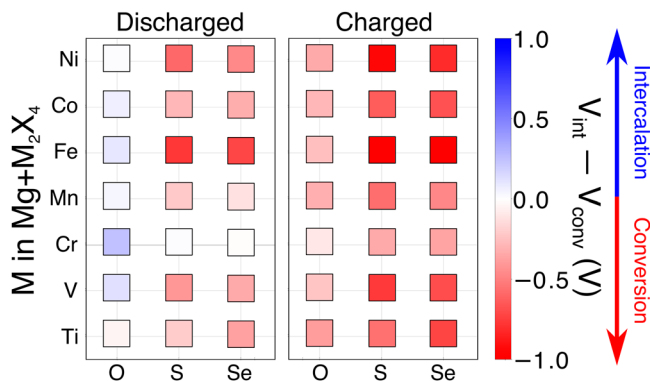


Figure 4.9 Difference between the intercalation and conversion voltages for Mg reduction in M_2X_4 cathodes, where $M = 3d$ transition metal and $X = O, S, \text{ or } Se$. Left and right panels correspond to reduction reactions using the lowest energy of the discharged and charged polymorphs. Adapted from ref. 21 with permission from John Wiley and Sons, © 2018 WILEY-VCH Verlag GmbH & Co. KGaA, Weinheim.

charged polymorph is considered (right panel). Hence, this analysis highlights three important trends: (i) oxides resist conversion better than sulphides and selenides, (ii) discharged polymorphs favour intercalation, (iii) Cr resists conversion to the largest degree among the 3d metals.

4.1.4.4 Co-intercalation in Xerogel- V_2O_5

Ref. 22 reports the impact of solvent co-intercalation under various electrolyte conditions for Mg discharge within xerogel- V_2O_5 , which is plotted in Figure 4.10. Using a three-step computational strategy to resolve the xerogel- V_2O_5 structure, Sai Gautam *et al.*²² calculated Mg intercalation voltages using the grand-potential (of Section 4.1.4) at various Mg concentrations and electrolyte conditions (*i.e.* a_{H_2O}). The authors reported that at low Mg concentrations ($x_{Mg} \leq 0.25$, red line in Figure 4.10), water co-intercalation is thermodynamically favoured in both wet ($a_{H_2O} \sim 1$) and dry ($a_{H_2O} \sim 10^{-4}$) electrolytes, as indicated by the linear dependence of voltages on a_{H_2O} . Water co-intercalation occurs only under wet conditions at higher Mg concentrations ($0.25 \leq x_{Mg} \leq 0.5$, blue line in Figure 4.10). Interestingly, a “superdry” electrolyte ($a_{H_2O} \sim 10^{-8}$) suppresses water co-intercalation (no dependence of voltage on a_{H_2O}) and removes any existing water from the xerogel structure (see equation, $0 \leftrightarrow 0$). Superdry electrolytes also alter the phase behaviour of the xerogel, signified by the merging of the low and high Mg voltage curves in Figure 4.10. Therefore, water co-intercalation and the dependence of the intercalation voltage on electrolyte conditions have important consequences in the choice of electrode/electrolyte pairs, where theoretical studies, such as in ref. 22, can provide important insights for experiments.

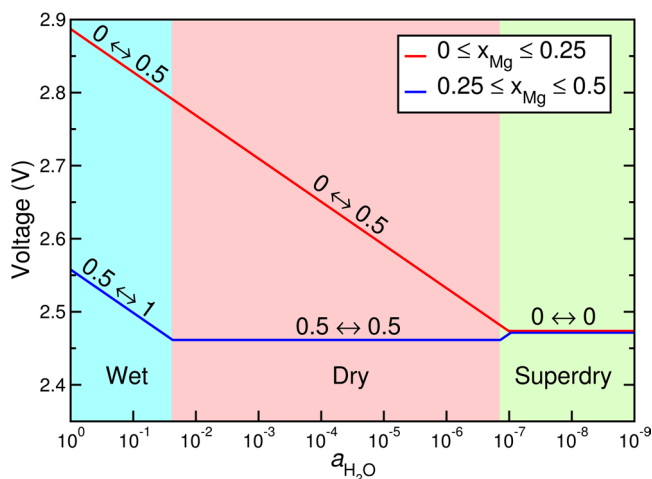


Figure 4.10 Average Mg intercalation voltages *vs.* Mg^{2+}/Mg at high (blue) and low (red) Mg concentrations as a function of water activity within the electrolyte. Equations along the voltage lines indicate the change in water content per V_2O_5 formula unit. Reproduced from ref. 22 with permission from the American Chemical Society, Copyright 2016.

4.1.4.5 Electrochemical Stability Windows of Coating Materials

A number of reports^{6,7,75} have clearly demonstrated that Mg electrolytes display a limited ESW (~ 1.5 V– 3.0 V *vs.* Mg) compared to Li-electrolytes (~ 1.5 V– 5 V *vs.* Li).⁷⁶ Thus, using protective anodic/cathodic coatings is one strategy to mitigate the poor ESW of Mg electrolytes. Chen *et al.*⁷⁷ predicted the EWS of several Mg-containing compounds, which may form as a result of electrolyte decomposition at either the Mg metal anode or high-voltage cathodes. The authors presented an exhaustive study of binary, ternary, and quaternary chemical spaces that contain non-redox-active metals (or cations) and anions.

Figure 4.11 depicts ESWs (using the framework in Section 4.1.5) of Mg ternary and quaternary oxides. Left (right) end of each bar indicates the reductive (oxidative) stability, with the number near each bar signifying the ESW. The voltage scale is referenced to Mg^{2+}/Mg , *i.e.* 0 V is Mg metal while ~ 3.5 V is $\text{Mg}_x\text{Cr}_2\text{O}_4$ (see Section 4.4.2). Interestingly, none of the Mg ternary (or quaternary) oxides are stable against Mg metal, as indicated by the lack of reductive stability of any compound up to 0 V, with $\text{Mg}(\text{BH}_4)_2$ (not shown in Figure 4.11) exhibiting the best reductive stability (0.01 V *vs.* Mg) among ternary Mg-compounds. Ternary oxides do not supersede the anodic stability of MgF_2 (~ 5.8 V,⁷⁷ not shown in Figure 4.11), with $\text{MgP}_4\text{O}_{11}$ (~ 4.55 V), MgS_2O_7 (~ 4.45 V), and quaternary $\text{Mg}_{0.5}\text{Ti}_2(\text{PO}_4)_3$ (~ 3.82 V) displaying high enough oxidative stabilities (>3.5 V) that could be compatible with high voltage cathodes. As noted in ref. 77, Mg mobility in these compounds needs to be assessed (see the examples in Section 4.4.6) before practical coating strategies can be implemented.

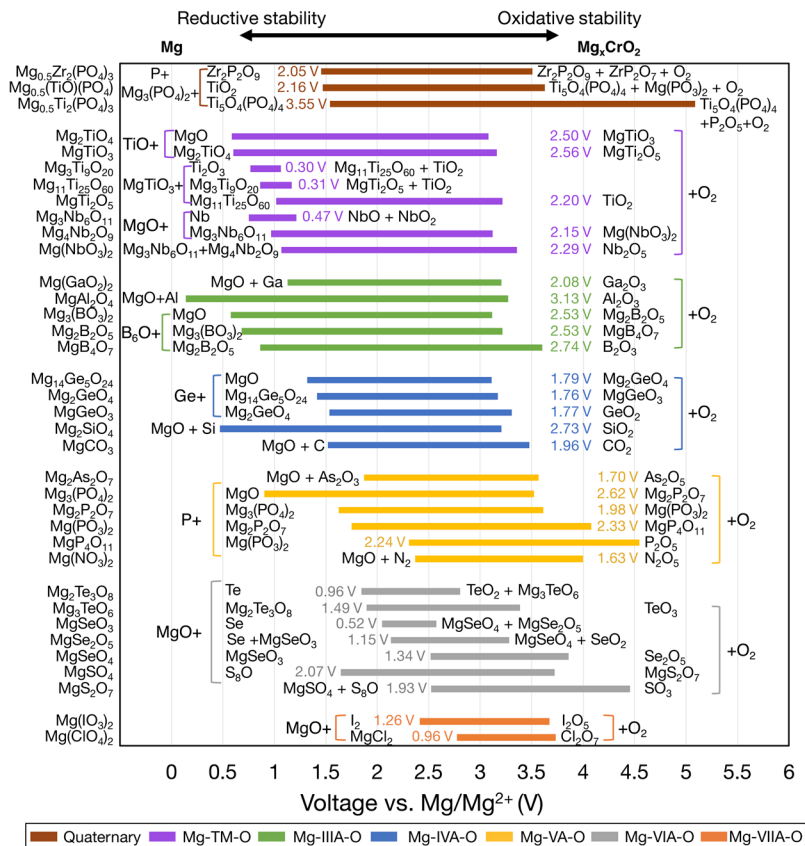


Figure 4.11 ESW of Mg-containing ternary and quaternary oxides as indicated next to each bar. The voltages (vs. Mg metal) across which the compound is stable is indicated by the width of each bar. Adapted from ref. 77, <https://doi.org/10.3389/fchem.2019.00024>, under the terms of the CC BY 4.0 licence, <https://creativecommons.org/licenses/by/4.0/>.

4.1.4.6 Assessing Mg Migration in a Spinel Structure

Here, we will examine the prediction of Mg migration barriers in a number of hosts exhibiting the spinel structure (Figure 4.12) using the methods in Section 4.2. Before delving into Mg migration, it is important to define an upper-limit of the migration barrier that electrodes can tolerate. As demonstrated previously,^{1,2,5} by assuming reasonable battery performance, e.g. a 2 h (dis)charge time t for a particle of active materials of a size of 1 μm (diffusion length), one arrives to a minimum required Mg diffusivity, $D \sim 10^{-12} \text{ cm}^2 \text{ s}^{-1}$, since the diffusion length scales as \sqrt{Dt} . If it assumed that a random-walk model for ion diffusion holds, $v \approx 10^{12} \text{ s}^{-1}$ and $a \approx 3 \text{ \AA}$, using eqn (4.21), one defines a maximum $\Delta E_a \sim 525 \text{ meV}$. In nanoparticle cathodes operating at a higher temperature ($\sim 60 \text{ }^\circ\text{C}$), the maximum ΔE_a can go up to $\sim 750 \text{ meV}$.⁵

The accuracy of computed barriers is typically ± 50 meV, which represents ~ 1 order of magnitude in diffusivity.

In spinel- MgM_2X_4 , the cation Mg and M order in a face-centred cubic (FCC) packing of anions X, as in Figure 4.12a. In “normal” spinels, $\frac{1}{2}$ of the octahedral (oct) 16d sites are M atoms (*e.g.* Ti or Mn, blue polyhedra), while $\frac{1}{8}$ of the tetrahedral (tet) 8a sites are Mg ions (orange polyhedra). Depending on the ionic radii of Mg^{2+} and $\text{M}^{2+/3+/4+}$, the spinel structure can exhibit “inversion”, where a fraction of the 8a (16d) sites are occupied by M (Mg) atoms. An extensive account of the spinel structure is given in ref. 78.

In screening for high-voltage oxide spinel cathodes, Liu *et al.*² calculated the Mg migration barriers in $\text{Mg}_x\text{M}_2\text{O}_4$ (M = Mn, Co, Ni or Cr) with DFT-NEB calculations (see Section 4.2.3). The MEP in $\text{Mg}_x\text{M}_2\text{O}_4$ follows a tet(8a) \rightarrow oct(16c) \rightarrow tet(8a) topology (top left in Figure 4.13), with the barrier often determined by the size of the triangular face shared by the 8a and 16c sites (bottom left in Figure 4.13). The authors demonstrated that the specific choice of M does not affect the energy landscape during migration with the calculated barriers being (charged–discharged limits) 776–486 meV for $\text{Mg}_x\text{Mn}_2\text{O}_4$, 698–520 meV for $\text{Mg}_x\text{Co}_2\text{O}_4$, 669–485 meV for $\text{Mg}_x\text{Ni}_2\text{O}_4$, and 616–636 meV for $\text{Mg}_x\text{Cr}_2\text{O}_4$. These barriers are larger in magnitude than for spinel- TiS_2 (~ 550 meV, Figure 4.12b), which can be attributed to the strong ionic bonding and electrostatic interactions between Mg^{2+} and O^{2-} .

Apart from calculating voltages, the authors in ref. 66 predicted the Mg migration barriers into spinel- TiS_2 , which were later shown to reversibly intercalate Mg experimentally by Sun *et al.*⁷² In spinel- TiS_2 , experiments⁷² have shown that a significant concentration of Mg ($x \sim 0.6$ per f.u.) resides in the usually-vacant oct sites, 16c (dashed square in Figure 4.12a). Therefore,

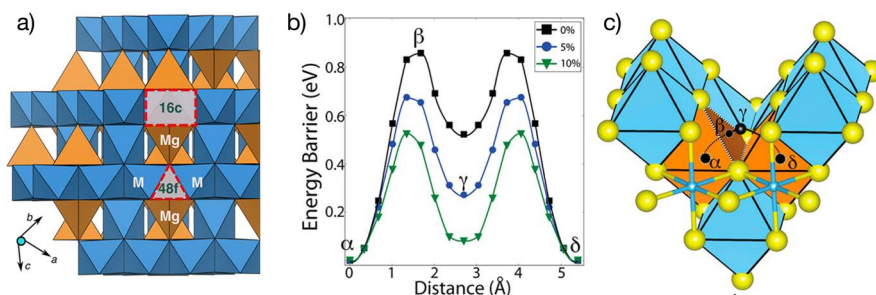


Figure 4.12 (a) Layout of Mg, M and X ions in the spinel structure MgM_2X_4 , where M is a transition metal and X the anion (O^{2-} , S^{2-} or Se^{2-}). Blue and orange polyhedra represent the M (16d, oct) and Mg (8a, tet) sites. Dashed rectangles and triangles indicate the vacant 16c (oct) sites and 48f (tet) sites, respectively. Adapted from ref. 4 with permission from the American Chemical Society, Copyright 2017. (b) NEB energy barrier of Mg^{2+} migration in MgTiS_2 , at different volumes and in the high vacancy limit. (c) Topology of Mg migration in MgTiS_2 , where α and δ are the 16c sites, and γ is the 8a site. Adapted from ref. 66 with permission from the American Chemical Society, Copyright 2015.

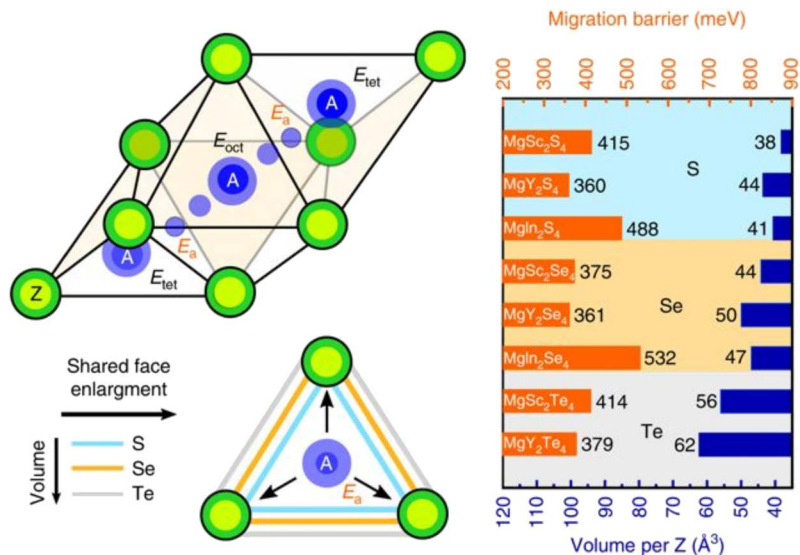


Figure 4.13 Right panel, calculated Mg migration barriers (orange bars) and the volume per anion (blue) in chalcogenides MgM_2Z_4 spinels. Top-left panel, typical tet \rightarrow oct \rightarrow tet migration path in spinels, with the energy of corresponding sites indicated by E_{tet} , and E_{oct} . E_a is the migration barrier. Bottom-left panel, representation of the effect of anion size on the triangular face shared between the 8a and 16c sites. Adapted from ref. 23, <https://doi.org/10.1038/s41467-017-01772-1>, under the terms of the CC BY 4.0 licence, <https://creativecommons.org/licenses/by/4.0/>.

the authors⁶⁶ assumed that the Mg^{2+} ions in spinel- TiS_2 migrate between 16c sites (α and δ in Figure 4.12c) *via* a local energy minima, the tet 8a site, where β in Figure 4.12c indicates the triangular face sharing site. The calculated barriers have been computed in the high vacancy limit – only one 16c amongst the 32 available in the lattice model is occupied by Mg. The calculated migration barriers decrease significantly from ~ 0.85 to ~ 0.55 eV as the volume increases by 10% from equilibrium (Figure 4.12b). These barriers are overestimated compared to values from galvanostatic intermittent titration experiments (~ 550 meV) and theory (500–600 meV) by Sun *et al.*,⁷² which could be due to the specific XC functional used in the NEB calculations.

Based on Mg migration barriers of a variety of cathode hosts, three practical design rules were developed by Rong *et al.* to identify good Mg conductors:^{1,24}

1. *Avoid materials with preferred Mg coordination.* A statistical analysis of the Inorganic Crystal Structural Database demonstrates that Mg highly prefers an octahedral coordination in oxides.^{1,2,79} Hence, materials where Mg does not occupy octahedral sites should be preferred.^{1,24}

2. *Limiting changes to ionic coordination.*¹ Smaller changes in coordination environment along the migration path flattens the energy landscape, and should reduce barriers.^{1,80}
3. *Increase volume per anion.* Larger anion volumes correlate with weaker electrostatic interactions of Mg with the anion and consequently reduce barriers.^{24,32}

Canepa *et al.*²⁴ applied these rules to identify the first class of room-temperature Mg ionic conductors, which are ternary spinel-MgM₂X₄, where M = In, Y or Sc and X = S or Se. Figure 4.13 depicts the computed barriers (orange bars) along the 8a → 16c → 8a (tet → oct → tet) pathway and volume per anion (per S²⁻ and Se²⁻, blue bars) in these materials. The barriers in Figure 4.13 are lower compared to those of cathode sulphur spinels (*e.g.* ~550 meV in MgTi₂S₄), with MgY₂S₄ (~360 meV), MgY₂Se₄ (~361 meV), and MgSc₂Se₄ (~375 meV) exhibiting the lowest barriers among the spinels considered. For MgSc₂Se₄,²⁴ impedance and variable-temperature ²⁵Mg NMR measurements were used to validate the theoretical predictions. However, impedance experiments measured non-negligible electronic conductivity, detrimental to the utilization of MgSc₂Se₄ as a Mg solid electrolyte. Subsequent theory investigations revealed that the chalcogenide spinels are prone to *n*-type conductivity, especially when synthesized under anion-poor environments (or high temperatures).⁸¹

4.1.4.7 Probing Long-range Mg Transport with Percolation Theory

In Section 4.2.4 we introduced the percolation theory, which was used to predict conditions under which long-range Mg transport occurs in spinel-Mg_xMn₂O₄, a potential cathode for Mg batteries^{2,71} but prone to inversion (see Section 4.4.6). A number of possible Mg migration pathways can be envisioned in inverted Mg_xMn₂O₄, and a complete description of these is given in ref. 4. A barrier of 750 meV was used as the defining criterion to classify active and inactive migration pathways, *i.e.* pathways that have barriers below (above) 750 meV facilitate or open (block or close) Mg migration. Within the percolation theory, sites in the spinel that are connected by open pathways (<750 meV barrier) are considered connected and can eventually form a contiguous percolating network.

Figure 4.14a displays the percolation threshold (x_{crit} , black lines), at various degrees of inversion (i) in Mn_{3-x}O₄ and various Mg vacancy concentrations (z). The x -axis starts at a Mn₃O₄ (*i.e.* 50% Mn-excess or 100% Mg-deficient) composition and covers Mg concentrations up to Mg_{1.5}Mn_{1.5}O₄ (*i.e.* 25% Mn-deficient, 50% Mg-excess). The dashed yellow line identifies the stoichiometric spinel (*i.e.* Mn:O = 2:4). The blue (red) coloured region signifies Mg concentrations which do (do not) facilitate percolation. In general, percolation thresholds in the Mn-excess domain (*i.e.* $x_{\text{crit}} < 1$) are desirable since they signify the presence of percolating networks in the stoichiometric spinel.

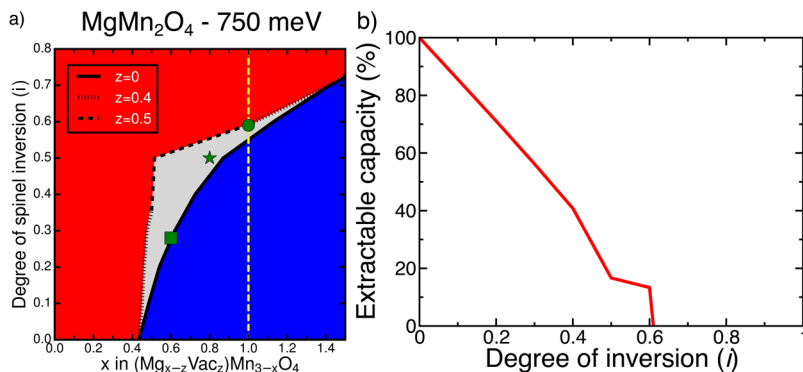


Figure 4.14 (a) Critical concentration (x_{crit}) of Mg percolation in $(\text{Mg}_{x-z}\text{Vac}_z)\text{Mn}_{3-x}\text{O}_4$. The stoichiometric concentration of $(\text{Mg}_{x-z}\text{Vac}_z)\text{Mn}_{3-x}\text{O}_4$ ($\text{Mn}:\text{O} = 2:4$) is illustrated by the yellow line. The zero on the x -axis indicates the Mn_3O_4 composition. z indicates the vacancy (Vac) concentration in $(\text{Mg}_{x-z}\text{Vac}_z)\text{Mn}_{3-x}\text{O}_4$. (b) The extractable Mg content (or capacity) for a stoichiometric Mn-oxide spinel as a function of the degree of inversion. Adapted from ref. 4 with permission from the American Chemical Society, Copyright 2017.

At $i = 0$, the stoichiometric spinel (yellow line) allows Mg percolation since the threshold ($x_{\text{crit}} \approx 0.44$) is in the Mn-excess domain. The stoichiometric discharged spinel ($z = 0$) can tolerate $i \sim 0.55$ before percolation stops, while a charged stoichiometric spinel ($z = 0.5$) enables Mg transport up to $i \sim 0.59$. Also, long-range Mg diffusion can be achieved at higher degrees of inversion ($0.59 < i < 0.77$) only under Mn-deficient concentrations (*i.e.* $x > 1$). Furthermore, the extractable Mg content (or the measured electrochemical capacity) from the Mn-oxide spinel is plotted as a function of i in Figure 4.14b for a stoichiometric spinel. Note that the extractable capacity decreases continuously with i , signifying the increasing number of Mg atoms that form isolated clusters within the spinel and hence do not participate in long-range diffusion. Finally, the extractable capacity reaches zero at $i \sim 0.6$, which corresponds to the highest degree of inversion that a stoichiometric spinel can tolerate before Mg percolation stops (Figure 4.14a). Thus, percolation theory can act as a robust theoretical framework to translate calculated microscopic migration barriers into long-range macroscopic transport properties.

4.2 Conclusions

The development of high energy density Mg batteries has been constrained by the lack of high voltage cathodes with good enough Mg mobility and reliable electrolytes that are stable against Mg metal and a high voltage cathode. Materials discovery, specifically using theory and computations to screen a variety of chemical spaces is required to make intercalation Mg batteries a reality. Here, we have introduced concepts of thermodynamics and kinetics

that are relevant for battery materials, briefly overviewed the levels of approximations used in the electronic structure methods (with a focus on DFT) to assess material properties and demonstrated practical examples where accurate properties have been calculated and benchmarked against experiments. We have also discussed examples where a high-throughput computational infrastructure has been used to screen for conversion-resistant cathodes, stable coating materials (and Mg ionic conductors) and formulate design principles that govern Mg mobility within typical solid frameworks. However, the hunt for reliable cathodes, coatings, and electrolytes for practical Mg and multivalent batteries is still ongoing. We hope that this chapter will provide sufficient guidance to the entire scientific community on the materials properties that can be accurately predicted theoretically, which should help in the screening and/or understanding of novel materials for high energy density Mg batteries.

Acknowledgement

P. C. acknowledges support from the Singapore Ministry of Education Academic Fund Tier 1 (R-284-000-186-133).

References

1. Z. Rong, R. Malik, P. Canepa, G. Sai Gautam, M. Liu, A. Jain, K. Persson and G. Ceder, *Chem. Mater.*, 2015, **27**, 6016.
2. M. Liu, Z. Rong, R. Malik, P. Canepa, A. Jain, G. Ceder and K. A. Persson, *Energy Environ. Sci.*, 2015, **8**, 964.
3. D. Aurbach, Z. Lu, A. Schechter, Y. Gofer, H. Gizbar, R. Turgeman, Y. Cohen, M. Moshkovich and E. Levi, *Nature*, 2000, **407**, 724.
4. G. Sai Gautam, P. Canepa, A. Urban, S.-H. Bo and G. Ceder, *Chem. Mater.*, 2017, **29**, 7918.
5. P. Canepa, G. Sai Gautam, D. C. Hannah, R. Malik, M. Liu, K. G. Gallagher, K. A. Persson and G. Ceder, *Chem. Rev.*, 2017, **117**, 4287.
6. H. D. Yoo, I. Shterenberg, Y. Gofer, G. Gershinsky, N. Pour and D. Aurbach, *Energy Environ. Sci.*, 2013, **6**, 2265.
7. J. Muldoon, C. B. Bucur and T. Gregory, *Chem. Rev.*, 2014, **114**, 11683.
8. P. Canepa, S. Jayaraman, L. Cheng, N. N. Rajput, W. D. Richards, G. S. Gautam, L. A. Curtiss, K. A. Persson and G. Ceder, *Energy Environ. Sci.*, 2015, **8**, 3718.
9. A. Ponrouch, C. Frontera, F. Bardé and M. R. Palacín, *Nat. Mater.*, 2016, **15**, 169.
10. P. Canepa, G. S. Gautam, R. Malik, S. Jayaraman, Z. Rong, K. R. Zavadil, K. Persson and G. Ceder, *Chem. Mater.*, 2015, **27**, 3317.
11. M. K. Aydinol, A. F. Kohan and G. Ceder, *J. Power Sources*, 1997, **68**, 664.
12. P. Hohenberg and W. Kohn, *Phys. Rev.*, 1964, **136**, B864.
13. W. Kohn and L. J. Sham, *Phys. Rev.*, 1965, **140**, A1133.

14. N. W. Ashcroft and N. D. Mermin, *Solid State Physics*, Cengage Learning, Inc, CA, United States, 1st edn, 1976.
15. C. Kittel, *Introduction to Solid State Physics*, John Wiley & Sons Inc, New York, United States, 8th edn, 2004.
16. D. A. McQuarrie and J. D. Simon, *Physical Chemistry: A Molecular Approach*, University Science Books, Sausalito, United States, 1st edn, 2011.
17. A. van de Walle and G. Ceder, *Rev. Mod. Phys.*, 2002, **74**, 11.
18. J. M. Sanchez, F. Ducastelle and D. Gratias, *Phys. A*, 1984, **128**, 334.
19. G. Ceder, *Comput. Mater. Sci.*, 1993, **1**, 144.
20. S. K. Kolli and A. Van der Ven, *Chem. Mater.*, 2018, **30**, 2436.
21. D. C. Hannah, G. Sai Gautam, P. Canepa and G. Ceder, *Adv. Energy Mater.*, 2018, **8**, 1800379.
22. G. Sai Gautam, P. Canepa, W. D. Richards, R. Malik and G. Ceder, *Nano Lett.*, 2016, **16**, 2426.
23. W. D. Richards, L. J. Miara, Y. Wang, J. C. Kim and G. Ceder, *Chem. Mater.*, 2016, **28**, 266.
24. P. Canepa, S.-H. Bo, G. Sai Gautam, B. Key, W. D. Richards, T. Shi, Y. Tian, Y. Wang, J. Li and G. Ceder, *Nat. Commun.*, 2017, **8**, 1759.
25. A. Van der Ven, G. Ceder, M. Asta and P. D. Tapesch, *Phys. Rev. B*, 2001, **64**, 184307.
26. D. Sheppard, R. Terrell and G. Henkelman, *J. Chem. Phys.*, 2008, **128**, 134106.
27. G. Henkelman, B. P. Uberuaga and H. Jónsson, *J. Chem. Phys.*, 2000, **113**, 9901–9904.
28. G. Henkelman and H. Jónsson, *J. Chem. Phys.*, 2000, **113**, 9978.
29. *Hans Hellmann: Einführung in die Quantenchemie*, ed. D. Andrae, Springer Berlin Heidelberg, Berlin, Heidelberg, 2015.
30. R. P. Feynman, *Phys. Rev.*, 1939, **56**, 340.
31. R. M. Martin, *Electronic Structure*, Cambridge University Press, Cambridge, 2004.
32. Y. Wang, W. D. Richards, S. P. Ong, L. J. Miara, J. C. Kim, Y. Mo and G. Ceder, *Nat. Mater.*, 2015, **14**, 1026.
33. S. P. Ong, V. L. Chevrier, G. Hautier, A. Jain, C. Moore, S. Kim, X. Ma and G. Ceder, *Energy Environ. Sci.*, 2011, **4**, 3680.
34. Z. Rong, D. Kitchaev, P. Canepa, W. Huang and G. Ceder, *J. Chem. Phys.*, 2016, **145**, 074112.
35. S. Adams and R. P. Rao, *Phys. Status Solidi*, 2011, **208**, 1746.
36. S. Adams and R. P. Rao, *Phys. Chem. Chem. Phys.*, 2009, **11**, 3210.
37. Y. Nishitani, S. Adams, K. Ichikawa and T. Tsujita, *Solid State Ionics*, 2018, **315**, 111.
38. F. Meutzner, T. Nestler, M. Zschornak, P. Canepa, G. S. Gautam, S. Leoni, S. Adams, T. Leisegang, V. A. Blatov and D. C. Meyer, *Phys. Sci. Rev.*, 2018, **4**, 20180044.
39. M. B. Isichenko, *Rev. Mod. Phys.*, 1992, **64**, 961.
40. J. W. Essam, *Rep. Prog. Phys.*, 1980, **43**, 833.
41. A. Urban, J. Lee and G. Ceder, *Adv. Energy Mater.*, 2014, **4**, 1400478.
42. S. C. van der Marck, *Int. J. Mod. Phys. C*, 1998, **09**, 529.

43. C. D. Lorenz and R. M. Ziff, *Phys. Rev. E*, 1998, **57**, 230.
44. W. Koch and M. C. Holthausen, *A Chemist's Guide to Density Functional Theory*, Wiley-VCH Verlag GmbH, Weinheim, FRG, 2001.
45. J. P. Perdew, in *AIP Conference Proceedings*, AIP, 2001, vol. 577, p. 1.
46. J. P. Perdew and A. Zunger, *Phys. Rev. B*, 1981, **23**, 5048.
47. J. P. Perdew, K. Burke and M. Ernzerhof, *Phys. Rev. Lett.*, 1996, **77**, 3865.
48. J. Sun, A. Ruzsinszky and J. Perdew, *Phys. Rev. Lett.*, 2015, **115**, 1.
49. F. Zhou, M. Cococcioni, C. A. Marianetti, D. Morgan and G. Ceder, *Phys. Rev. B*, 2004, **70**, 235121.
50. V. I. Anisimov, J. Zaanen and O. K. Andersen, *Phys. Rev. B*, 1991, **44**, 943.
51. S. P. Ong, L. Wang, B. Kang and G. Ceder, *Chem. Mater.*, 2008, **20**, 1798.
52. T. Chen, G. Sai Gautam, W. Huang and G. Ceder, *Chem. Mater.*, 2018, **30**, 153.
53. G. Sai Gautam, P. Canepa, A. Abdellahi, A. Urban, R. Malik and G. Ceder, *Chem. Mater.*, 2015, **27**, 3733.
54. G. Sai Gautam and E. A. Carter, *Phys. Rev. Mater.*, 2018, **2**, 095401.
55. P. Pernot, B. Civalleri, D. Presti and A. Savin, *J. Phys. Chem. A*, 2015, **119**, 5288.
56. F. Corà, M. Alfredsson, G. Mallia, D. S. Middlemiss, W. C. Mackrodt, R. Dovesi and R. Orlando, *The Performance of Hybrid Density Functionals in Solid State Chemistry*, in *Principles and Applications of Density Functional Theory in Inorganic Chemistry II*, Springer, Berlin, Heidelberg, 2004, pp. 171.
57. A. D. Becke, *J. Chem. Phys.*, 1993, **98**, 5648.
58. C. Lee, C. Hill and N. Carolina, *Chem. Phys. Lett.*, 1989, **162**, 165.
59. P. J. Stephens, F. J. Devlin, C. F. Chabalowski and M. J. Frisch, *J. Phys. Chem.*, 1994, **98**, 11623.
60. C. Adamo and V. Barone, *J. Chem. Phys.*, 1999, **110**, 6158.
61. J. Heyd, G. E. Scuseria and M. Ernzerhof, *J. Chem. Phys.*, 2003, **118**, 8207.
62. J. Heyd and G. E. Scuseria, *J. Chem. Phys.*, 2004, **121**, 1187.
63. A. Jain, G. Hautier, S. P. Ong, C. J. Moore, C. C. Fischer, K. a. Persson and G. Ceder, *Phys. Rev. B*, 2011, **84**, 045115.
64. L. Wang, T. Maxisch and G. Ceder, *Phys. Rev. B*, 2006, **73**, 195107.
65. V. L. Chevrier, S. P. Ong, R. Armiento, M. K. Y. Chan and G. Ceder, *Phys. Rev. B*, 2010, **82**, 075122.
66. A. Emly and A. Van der Ven, *Inorg. Chem.*, 2015, **54**, 4394.
67. T. A. Barnes, L. F. Wan, P. R. C. Kent and D. Prendergast, *Phys. Chem. Chem. Phys.*, 2018, **20**, 24877.
68. A. Jain, S. P. Ong, G. Hautier, W. Chen, W. D. Richards, S. Dacek, S. Cholia, D. Gunter, D. Skinner, G. Ceder and K. A. Persson, *APL Mater.*, 2013, **1**, 011002.
69. W. Sun, S. T. Dacek, S. P. Ong, G. Hautier, A. Jain, W. D. Richards, A. C. Gamst, K. A. Persson and G. Ceder, *Sci. Adv.*, 2016, **2**, e1600225.
70. N. Amir, Y. Vestfrid, O. Chusid, Y. Gofer and D. Aurbach, *J. Power Sources*, 2007, **174**, 1234.

71. C. Kim, P. J. Phillips, B. Key, T. Yi, D. Nordlund, Y.-S. Yu, R. D. Bayliss, S.-D. Han, M. He, Z. Zhang, A. K. Burrell, R. F. Klie and J. Cabana, *Adv. Mater.*, 2015, **27**, 3377.
72. X. Sun, P. Bonnick, V. Duffort, M. Liu, Z. Rong, K. A. Persson, G. Ceder and L. F. Nazar, *Energy Environ. Sci.*, 2016, **9**, 2273.
73. X. Sun, P. Bonnick and L. F. Nazar, *ACS Energy Lett.*, 2016, **1**, 297.
74. G. Gershinsky, H. D. Yoo, Y. Gofer and D. Aurbach, *Langmuir*, 2013, **29**, 10964.
75. A. L. Lipson, S.-D. Han, B. Pan, K. A. See, A. A. Gewirth, C. Liao, J. T. Vaughey and B. J. Ingram, *J. Electrochem. Soc.*, 2016, **163**, A2253.
76. J. B. Goodenough and Y. Kim, *Chem. Mater.*, 2010, **22**, 587.
77. T. Chen, G. Ceder, G. Sai Gautam and P. Canepa, *Front. Chem.*, 2019, **7**, 24.
78. K. E. Sickafus, J. M. Wills and N. W. Grimes, *J. Am. Ceram. Soc.*, 1999, **82**, 3279.
79. I. D. Brown, *Acta Crystallogr., Sect. B: Struct. Sci.*, 1988, **44**, 545.
80. G. S. Gautam, P. Canepa, R. Malik, M. Liu, K. Persson and G. Ceder, *Chem. Commun.*, 2015, **51**, 13619.
81. P. Canepa, G. Sai Gautam, D. Broberg, S.-H. Bo and G. Ceder, *Chem. Mater.*, 2017, **29**, 9657.